THESIS FOR THE DEGREE OF DOCTOR OF PHILOSOPHY

Thermoelectric- and hot-electron effects in graphene devices

GRIGORY SKOBLIN

Department of Microtechnology and Nanoscience - MC2
CHALMERS UNIVERSITY OF TECHNOLOGY
Göteborg, Sweden 2017

Thermoelectric- and hot-electron effects in graphene devices
GRIGORY SKOBLIN
ISBN 978-91-7597-681-5

Doktorsavhandlingar vid Chalmers tekniska högskola
Ny serie nr 4362
ISSN 0346-718X

Quantum Device Physics Laboratory
Department of Microtechnology and Nanoscience - MC2
Chalmers University of Technology
SE–412 96 Göteborg
Sweden
Telephone +46 (0)31-772-1000

ISSN 1652-0769
Technical report MC2-378

Chalmers Reproservice
Göteborg, Sweden 2017

Thermoelectric- and hot-electron effects in graphene devices
GRIGORY SKOBLIN
Department of Microtechnology and Nanoscience (MC2)
Chalmers University of Technology, 2017
Göteborg, Sweden 2017

Abstract

A technology of encapsulation of graphene in Parylene was introduced as an alternative to encapsulating graphene in hBN. Edge contacts to the encapsulated graphene in this case showed resistivity down to 14 $\Omega \cdot \mu$m, which is the lowest reported value so far. The resulting graphene devices showed a high carrier mobility (up to 30000 cm^2/(V s) at 300K), low doping (down to 10^{11} cm^{-2}) and were stable in time. Possibility of encapsulating also CVD graphene for large-scale device fabrication was shown.

This Parylene encapsulation technology was used for fabrication of thermoelectric graphene devices and radiation detectors. Since the Seebeck coefficient in graphene is high, the thermoelectric effects are strong. A dual-gated design was used to create an intrinsic graphene thermocouple. Due to a weak coupling between phonons and electrons in graphene, the electrons can have significantly higher temperature than the phonons. These devices allowed for simple measurement of electron temperature in graphene. When coupled to an antenna, such a device served as a radiation detector. Even under unoptimized conditions the detectors showed responsivity up to 700 V/W and noise level down to 18 pW/Hz$^{0.5}$. The response time was estimated to be less than 1.2 ps.

Keywords: graphene, CVD, encapsulation, Parylene, thermoelectric effects, bolometer.

Appended papers

This thesis is based on the following papers:

I G. Skoblin, N. Lindvall, J. Sun, A. Yurgens, A Hybrid Type Chemical Vapor Deposition System for Graphene Growth, *Chem. Vap. Dep.* **21**, pp 176-180, 2015

II G. Skoblin, J. Sun and A. Yurgens, Encapsulation of graphene in Parylene, *Appl. Phys. Lett.* **110**, 053504, 2017

III G. Skoblin, J. Sun and A. Yurgens, Thermoelectric effects in graphene at high bias current and under microwave irradiation, *Sci. Rep.* **7**, 15542, 2017

IV G. Skoblin, J. Sun and A. Yurgens, Thermoelectric graphene bolometer with capacitive coupling to an antenna, accepted to *Appl. Phys. Lett.*

Other papers which are outside the scope of this thesis

- Z. Zhan, J. Sun, and L. Liu, E. Wang, Y. Cao, N. Lindvall, G. Skoblin, A. Yurgens, Pore-free bubbling delamination of chemical vapor deposited graphene from copper foils, *J. Mat. Chem. C* **3**, pp 8634-8641, 2015
- V.N. Glazkov, G. Skoblin, D. Hüvonen, T.S. Yankova, A. Zheludev, Formation of gapless triplets in the bond-doped spin-gap antiferromagnet $(C_4H_{12}N_2)(Cu_2Cl_6)$, *J. Phys. Cond. Matt.* **26**, 486002, 2014
- V.N. Glazkov, M. Fayzullin, Y. Krasnikova, G. Skoblin, D. Schmidiger, S. Mühlbauer, A. Zheludev, ESR study of the spin ladder with uniform Dzyaloshinskii-Moriya interaction, *Phys. Rev. B* **92**, 184403, 2015

Contents

1 Introduction

Carbon atoms are building units of nature. They can establish strong bonds between each other and a wide variety of possible combinations with other elements give us the whole science of organic chemistry. Even carbon itself can exist in several different allotropic forms. The two most known ones are graphite and diamond. Graphite is a layered material consisting of atomically thin sheets. If one such a sheet is isolated, it appears to be another allotrope due to substantially different properties compared to graphite. This allotrope is called graphene. Graphene drew attention after 2004 and 2005, when the first papers on experimental observation of its electronic properties were published and became known even outside the academic society after 2010 Nobel Prize had been given to A. Geim and K. Novoselov [1, 2, 3]. However, the first theoretical predictions on unique properties of atomically thin graphite came much earlier: in 1947 it was theoretically shown for the first time that one atomic sheet of graphite should have unusual semi-metallic behaviour and that the charge carriers should be as massless Dirac fermions [4]. It took more than half a century to prove these predictions experimentally. The main problems have been the lack of a reliable method of obtaining atomically thin graphite and a useful way to detect individual atomic layers. Few- and possibly monolayer graphite films were observed in soot after exploding carbon-containing materials [5, 6] by using scanning electron microscope (SEM).

Only in the beginning of XXI century these two problems were solved. A. Geim and K. Novoselov suggested a very simple technique of graphene exfoliation that allows to isolate monolayer flakes. They started from bulk graphite and used a sticky tape to separate its layers. Another bright idea was implemented to make graphene visible: oxidized silicon enhances the visibility of graphene deposited on it due to the interference effect [7]. Despite the small size of the exfoliated graphene flakes, many of their properties were measured [8, 9, 10]. Graphene's great potential for future applications was enhanced by discovery of the chemical vapor deposition (CVD) method to obtain large-scale monolayer graphene films on copper [11]. This method opened the road to mass production of graphene and stimulated its applications [12].

Graphene appears to have a wide variety of outstanding properties. It is a two-dimentional (2D) material with the thickness of 0.34[a] nm and area

---

[a] It is difficult to define the thickness of an atomically thin material. This value represents the vertical spacing between the layers in graphite and is usually taken in the calculations of the physical properties of graphene.

density of 0.38 mg/m^2. Its mechanical properties are impressive: it is stretchable to 25% and has one of the highest measured tensile strength - 130 GPa [9]. These mechanical properties can be used to create strong composites [13] and paper [14]. Graphene has thermal conductivity higher than 5000 W/(K m) [15]. This can be used in cooling systems for microcircuits [16]. Graphene is simultaneously a conductive and transparent material (absorbs $\sim$ 2.3% light [17]), which is an exceptional combination. This combination allows to use graphene as the transparent electrone for touch screens, which can potentially become flexible [18]. Graphene shows long spin coherence length (up to 12 μm [19]), which is very promising for spintronic applications. The highest measured charge-carrier mobility in graphene exceeds 10^6 cm^2/(V s) with mean free path of electrons up to 28 μm [20, 21]. This is used for demonstration of electron ballistic effects [22] and can be applied for ultra-sensitive Hall sensors [23].

Despite many possible applications, graphene has some serious drawbacks. Initially, there were hopes for graphene to completely replace silicon in microcircuits, making them even smaller and, possibly, flexible. However, monolayer graphene does not have a gap in the charge-carrier energy spectrum, which makes it impossible to fabricate efficient field-effect transistors; without a gap it is impossible to switch a transistor off. The performance of the existing graphene transistors is still lower than that of the silicon-based ones [24]. Bilayer graphene can have a gap in the spectrum if a vertical electric field is applied [25], but this gap is small compared to the gaps of the known semiconductors. It is also more difficult to produce high quality bilayer graphene than the monolayer [26, 27].

Graphene is not the only 2D material in the world. Hexagonal boron nitride (hBN), a 2D insulator, is widely used as a substrate and coverage for graphene [28]. Single layers of black phosphorus show many interesting and useful properties [29, 30]. There is a wide family of transition metal dichalcogenides, which are 2D semiconductors. They have been widely studied and also show high potential for future applications [31, 32, 33].

1.1 Aim and Outline

This thesis focuses on fabrication of graphene devices and investigation of thermoelectric- and hot-electron effects in them. The aim of this thesis is to demonstrate a scalable graphene encapsulation technology and its application for radiation detector fabrication. The results obtained in this work can be used for better understanding of the thermoelectric effects in graphene and can also be useful for industry in future.

Chapter 2 provides a brief description of the relevant fundamental properties of graphene.

Chapter 3 concerns the methods of graphene synthesis, discussion of the graphene CVD process and the systems used for it (**Paper I**).

Chapter 4 presents the technologies of graphene encapsulation: the well-known hBN-technology and developed in this work encapsulation in Parylene. The results from device fabrication and characterization are discussed (**Paper II**).

In Chapter 5 thermoelectric- and hot-electron effects in graphene are discussed. The performance of hot-electron graphene bolometers based on these effects is demonstrated (**Paper III** and **Paper IV**).

In Chapter 6 the results of computer modelling of a heater in a CVD system and a thermoelectric device are presented in addition to Chapters 3 and 5.

2 Theoretical background

2.1 Basic electronic properties of graphene

Graphene has remarkable electronic properties [34]. The low-energy charge-carriers are massless and have linear energy dispersion. The Brillouin zone has six-fold symmetry and has six points where the conduction- and valence bands meet, Dirac points (see Fig. 1). In close vicinity of these points the energy dispersion is the following:

$$E_{\pm} = \pm\hbar v_F |\mathbf{k}|, \tag{1}$$

where v_F is the Fermi velocity and $\mathbf{k}$ is the wave vector.

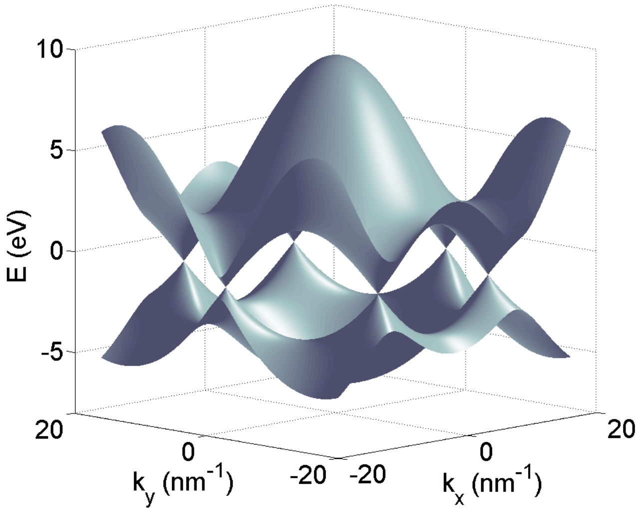

Figure 1: Carrier energy dispersion in graphene.

This spectrum defines the semimetallic behaviour of graphene: the conductivity in Dirac point is zero for the ideal case. However, any infinitely small deviation of Fermi level leads to a nonzero conductivity. In other words, due to the lack of gap in the spectrum, it is possible to "switch off" the conductivity in graphene only in the Dirac point. For nonideal samples, the Fermi level in graphene can be easily shifted by impurities on its surface [35, 36]. Since the impurities are distributed nonuniformly, they cause different local Fermi level shifts. Thus, for a real graphene sample it is impossible to have the zero conductivity. The dependence of conductivity on charge-carrier concentration can be approximated by [37]:

$$\sigma(n) = e\mu n_{tot} = e\mu\sqrt{n_0^2 + n^2}, \tag{2}$$

where e is the elementary charge, μ is the charge-carrier mobility, n_{tot} is the total carrier concentration, n_0 is the carrier density at the minimum conductivity, n is the externally induced carrier concentration. Here we use the Drude model of conductivity, which is usually sufficient to describe the experiments. Experimentally, the carrier concentration in graphene is tuned by a gate electrode, separated from the graphene by a dielectric. In this case, n is expressed as $n = (V_g - V_D)C_g/e$, where C_g is the specific capacitance between graphene and the gate electrode, V_g is the voltage applied to the gate and V_D is the shift of the Dirac point due to parasitic doping. The measurement of the so-called transfer characteristic curve - the dependence of graphene resistance on the back-gate voltage - is a common way to characterize a graphene device. This curve is usually fit by Eq. 2 in resistivity form:

$$R(V_g) = R_c + \frac{N_\square}{\mu\sqrt{(en_0)^2 + C_g^2(V_g - V_D)^2}}, \tag{3}$$

where R_c is the contact resistance and $N_\square = l/w$ is the number of squares along the device (the length divided by the width). After fitting, this single curve gives the information about doping (V_D), carrier density at the minimum conductivity (n_0), contact resistance, and gives an estimation of carrier mobility.

2.2 Basic thermal properties of graphene

The heat capacity C at high temperature in graphene comes, to the first approximation, from the Dulong - Petit law: $C = 3R$, where R is the universal gas constant. This agrees with numerical calculations [38]. However, at room temperature the heat capacitance of graphite is only $1.03R$. This can be explained by some of the vibrational modes having high energy and being not activated at room temperature. Thermal conductivity of graphene was measured for both suspended ($\kappa = 4800 - 5300$ W/(K m) [15]) and supported ($\kappa \sim 600$ W/(K m) [39]) graphene at room temperature.

The electrons also contribute to the heat transfer in graphene. Although they have noticeably lower heat capacitance C_e and heat conductance κ, these values can be measured experimentally [40]. For suspended graphene at room temperature: $C_e = 4.5 \times 10^{-3}$ J/(mol K) and $\kappa = 11$ W/(K m). These values correspond to the kinetic transport model $\kappa = \frac{1}{2}C_e v_F l_e$, where l_e is the electron mean free path ($l_e = n\mu h/2ek_F$ [41]).

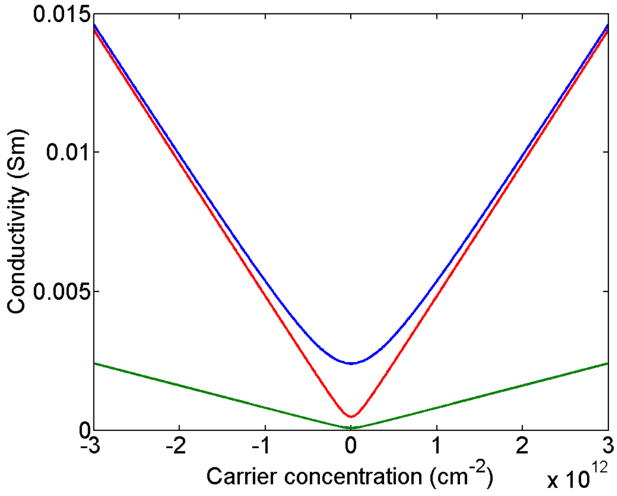

Figure 2: The plot of the Eq. 2 for different parameters. Red curve: $\mu = 30000$ cm^2/(V s), $n_0 = 1.0 \times 10^{11}$ cm^{-2}. Blue curve: $\mu = 30000$ cm^2/(V s), $n_0 = 5.0 \times 10^{11}$ cm^{-2}. Green curve: $\mu = 5000$ cm^2/(V s), $n_0 = 1.0 \times 10^{11}$ cm^{-2}.

One more interesting property is the coupling between phonons and electrons. It was observed, that this coupling is relatively weak [42, 43, 44]. The power exchange between electrons and phonons can be expressed as: $P_{e-ph} = A(T_e^m - T_{ph}^m)$, where T_e and T_{ph} are the electron- and phonon temperatures, respectively. The power m depends on the phonon temperature and is $m = 3$ for high temperatures and $m = 4$ for low temperatures. The Joule heat makes the electrons have higher temperature, than the phonons, especially at high bias current.

2.3 Thermoelectric properties of graphene

When both electric field and temperature gradient coexist in metals, the resulting electric current and the heat flow are interconnected according to the equations [45]:

$$\mathbf{E} = \rho \mathbf{J} + S \nabla T \tag{4}$$

$$\mathbf{q} = \Pi \mathbf{J} - \kappa \nabla T \tag{5}$$

where Π and S are the Peltier and Seebeck coefficients respectively. Due to Onsager's principle, there is a relation between them: $\Pi = ST$. Thermoelectric properties are usually defined by the value of S for a given material. In graphene, the Seebeck coefficient can reach values 100 μV/K, which is grater than for most metals. Moreover, because of tunability of charge-carrier concentration in graphene, the Seebeck coefficient can change value and sign. Its value can be expressed in terms of conductivity via Mott's relation:

$$S(T,\sigma) = -\frac{\pi^2}{3}\frac{k_B^2 T}{e}\frac{1}{\sigma}(\frac{\partial\sigma}{\partial\varepsilon})_{\varepsilon=\varepsilon_F} \quad (6)$$

The applicability of this formula in graphene is limited [46]. In this thesis we use it mainly for qualitative analysis. The plot of Eq. 6 is presented in Fig. 3. As seen from the plot, the sign of S depends on the carrier type, being positive for holes and negative for electrons.

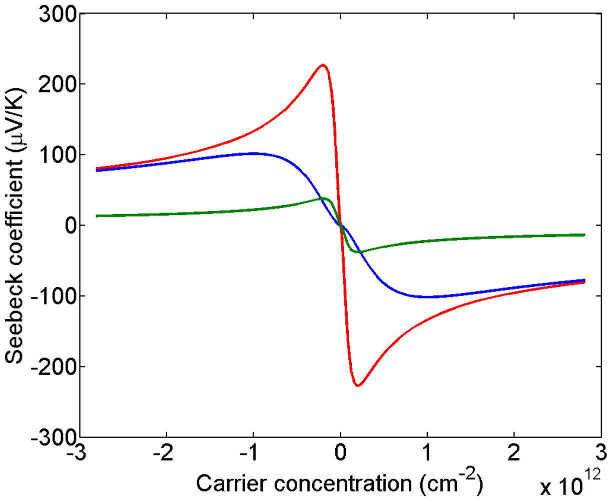

Figure 3: The Seebeck coefficient calculated from Mott's equation (Eq. 6) for different parameters. Red curve: $n_0 = 1.0 \times 10^{11}$ cm^{-2}, $T = 300$ K. Blue curve: $n_0 = 5.0 \times 10^{11}$ cm^{-2}, $T = 300$ K. Green curve: $n_0 = 1.0 \times 10^{11}$ cm^{-2}, $T = 50$ K.

2.4 Hall effect

In the classical Hall effect, the magnetic field creates a potential difference transverse to the current direction, which is called Hall voltage (V_H) and can be expressed as:

$$V_H = -\frac{IB}{qn} \quad (7)$$

where I is the current, q is the carrier charge and n is the carrier concentration. So, the Hall resistance $R_H = \frac{V_H}{I}$ appears to be proportional to the magnetic field with the Hall constant $-\frac{1}{qn}$. The Hall constant gives the sign of the charge-carriers and their concentration. It is possible to extract the carrier mobility from the Hall-effect measurement. From Eq. 2, the mobility equals $\mu = \frac{\sigma}{en_{tot}}$. After substituting the Hall constant we arrive at:

$$\mu = -\sigma \frac{dR_H}{dB} \tag{8}$$

where $\frac{dR_H}{dB}$ indicates the slope of the resistance curve. However, in two-dimensional (2D) systems (and so in graphene as well) the classical Hall effect occurs only in low magnetic fields (usually $< 1T$). In high magnetic fields and at low temperatures, quantum effects start to play role in 2D systems. For a 2D electron gas, the energy levels are quantized in magnetic field (they are also called Landau levels): $E_n = (n + \frac{1}{2})\hbar\omega_c$, $n = 1, 2, ...$ Therefore, the Hall conductivity is quantized as well, $\sigma_H = g_s(n + \frac{1}{2})\frac{e^2}{h}$, where $\frac{e^2}{h}$ is the conductance quantum, g_s is the system degeneracy, which equals 4 for monolayer graphene. The filling factor $\nu = g_s(n + \frac{1}{2})$ takes the values $\pm 2, \pm 6, \pm 10...$ for monolayer graphene.

2.5 Self gating effect in graphene

The self gating effect plays role when a device is biased to significantly high voltage, comparable with the back gate voltages used to change the carrier concentration. To describe this effect quantitatively, we consider a graphene rectangle of width w with one end biased to voltage V_0 and the other one grounded. The potential distribution along the current direction $V(x)$ obeys the following equations:

$$dV(x) = \frac{I dx}{\sigma(x) w} \tag{9}$$

$$\sigma(x) = \mu\sqrt{C_g^2 V(x)^2 + e^2 n_0^2} \tag{10}$$

After making this equation dimensionless by introducing $v(x) = \frac{C_g V(x)}{en_0}$ and $i(x) = \frac{C_g I}{\mu(en_0)^2}$, we get the following differential equation:

$$\sqrt{v^2 + 1} dv = \frac{i dx}{w}, \tag{11}$$

which can be solved analytically:

$$v(x)\sqrt{v^2(x) + 1} + ln(v(x) + \sqrt{v^2(x) + 1}) = \frac{2ix}{w} \tag{12}$$

The plot of $v(i)$ for $x = w$ is presented in Fig. 4. We see that the deviation of the current-voltage (IV) curve from the linear dependence starts to be significant for $i > 1$, which corresponds to $I > 100\mu A$ for usual experimental values: $C_g = 1.13 \times 10^{-4}$ F/m^2, $n_0 = 1.0 \times 10^{11}$ cm^{-2} and $\mu = 5000$ cm^2/(V s).

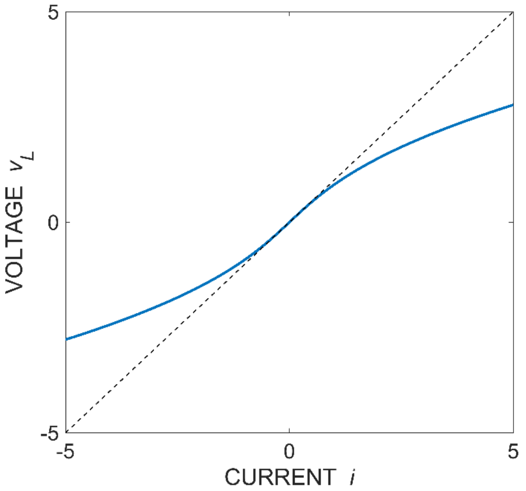

Figure 4: The plot of the Eq. 12 (solid line) in comparison with the straight ohmic IV line (dashed). Adopted from Supplementary for Paper **III**.

2.6 Raman spectroscopy of graphene

Raman spectroscopy is a useful tool for studying various materials [47]. A sample is illuminated with photons (a focused laser beam) and the inelastically scattered photons are collected and analysed. The shift of the wavelength between the sent- and the scattered photons provides information about the phonon modes existing in the sample. Raman spectrum represents the intensity of inelastically scattered photons as a function of their wavelength change (Raman shift).

For graphene, the Raman spectrum has three characteristic peaks (see Fig. 5). The G peak corresponds to the zone center mode and can be observed for other carbon containing materials; the 2D peak results from a double scattering of zone boundary phonons [48]. The D peak corresponds to the same zone boundary phonons as 2D peak, but comes from the single-phonon scattering event. It does not occur in pristine graphene lattice, but in presence of defects or near the graphene edges the symmetry breaks and the single-phonon scattering becomes allowed. Sometimes weak G* peak is also present in the spectrum, it also corresponds to double-phonon scattering as for the 2D peak, but it involves phonons from different bands [49].

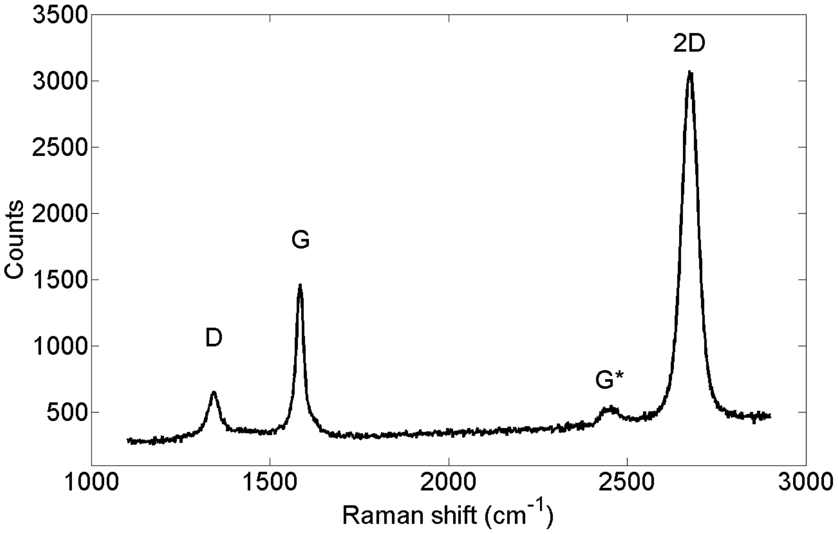

Figure 5: A representative Raman spectrum for monolayer graphene. The major characteristic peaks are D ($\sim$ 1340 cm^{-1}), G ($\sim$ 1585 cm^{-1}) and 2D ($\sim$ 2675 cm^{-1}). Sometimes small G* peak ($\sim$ 2450 cm^{-1}) is also observable.

Raman spectroscopy appears to be very practical for characterization of graphene samples. The density of defects in the lattice is indicated by the intensity of the D peak. Mechanical strain shifts the position of the G peak from the original, which allows to estimate possible deformations in the sample. For multilayer graphene, the 2D peak splits into several components, which together look like one asymmetric peak. This allows to distinguish monolayer graphene from multilayer graphene without fabricating electric devices from it.

3 Synthesis of graphene

3.1 Exfoliation

The first method to obtain graphene was mechanical exfoliation, implemented by Geim and Novoselov [1]. This method is fairly simple. A piece of natural graphite is several times cleaved using a sticky tape. Then, the sticky tape with random graphite flakes is pressed to the target substrate and peeled off. There is a chance that graphene sticks to the substrate and some monolayer flakes will thereby be transferred to the target substrate. The flakes are usually small, $15 - 20\ \mu m$. A typical optical image of exfoliated graphene is presented in Fig. 6.

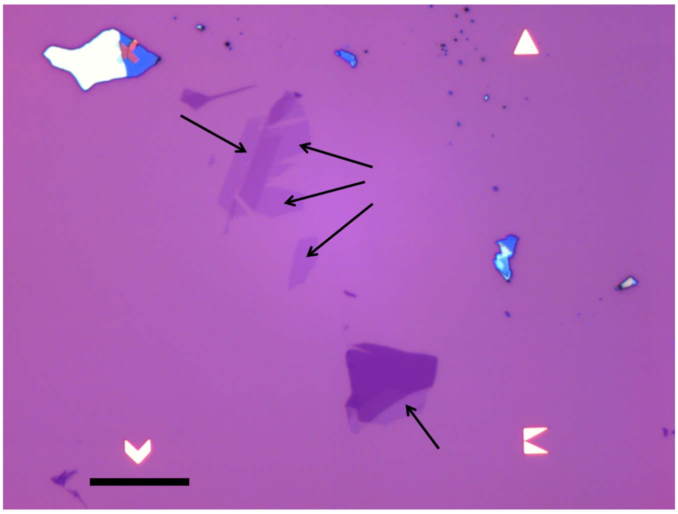

Figure 6: Graphene flakes exfoliated on SiO_2(285 nm)/Si chip. Arrows are pointing to the monolayer regions. The scalebar is 20 μm.

The most common substrate for graphene exfoliation is oxidized silicon. Due to interference effect, graphene flakes have a finite contrast on this substrate, which can be maximized for a certain oxide thickness. For green light, the monolayer graphene can have up to 10 % contrast[b] for the oxide thickness around 90 nm and 290 nm [7].

Exfoliation allows to quickly produce graphene flakes without a need for sophisticated equipment. The precursor for exfoliation can be either natural graphite or a man-made Highly Oriented Pyrolytic Graphite (HOPG).

---

[b] Contrast is defined as the ratio $\frac{I_{sub}-I_{gr}}{I_{sub}}$, where I_{sub} and I_{gr} are the amplitudes of the reflected light from the substrate and graphene, respectively.

Natural graphite usually results in graphene flakes of higher quality. The experimentally observed charge-carrier mobility in exfoliated samples can reach the theoretical limit [50]. However, since the size of the resulting flakes is limited, this technique is not scalable; it does not allow for mass production of devices.

3.2 Chemical vapor deposition

The need for an industrially applicable way to produce graphene motivated scientists to work in that direction. The discovery of the catalytic chemical vapor deposition (CVD) method brought graphene from labs to industry [11, 12, 51]. Graphene CVD occurs at high temperatures, usually on catalytic metal substrates. The most common catalyst for monolayer graphene growth appears to be copper. Nickel is also used as a substrate to grow graphene on, but due to a high carbon solubility in nickel, the resulting graphene is often a multilayer. Other metals like platinum, rhodium, etc. can also be used, but are expensive and thus less common.

The process of graphene CVD is a thermal decomposition of carbon-containing precursor at a catalyst surface and a subsequent formation of graphene. Methane is widely used as a precursor gas and in this case the simplified chemical reaction is the following:

$$\mathrm{CH_4} \xleftrightarrow{\text{800-1100 °C}} \mathrm{C} + 2\,\mathrm{H_2} - 75\,\mathrm{kJ} \tag{13}$$

A typical system for graphene growth has several gas inlets for Ar, CH_4 and H_2 and a possibility to heat up a sample up to 1000°C. The graphene CVD process consists of the following steps: heating up, annealing, growth and cooling down (see Fig. 7). Only Ar and H_2 are introduced into the chamber during the first two steps. The annealing step is needed to etch away remaining copper oxide from the surface ($\mathrm{Cu_2O} + \mathrm{H_2} \longrightarrow 2\,\mathrm{Cu} + \mathrm{H_2O}$), recrystallize the copper foil thus improving the surface roughness, and to stabilize the temperature distribution in the whole system. The growth of graphene is initiated by introducing CH_4 into the chamber. After a certain time, the heater is switched off and the chamber is cooled down to room temperature. The CH_4 can be shut off or kept on during the last step depending on the exact recipe.

The important parameters for graphene growth are temperature, gas flows, chamber pressure, annealing- and growth times. For monolayer graphene growth, the ratio between the CH_4 and H_2 partial pressures is usually between 1:100 and 1:5000 [11]. Therefore, very low ($\sim$1 sccm) CH_4 flows are required, which is difficult to achieve for pure CH_4 using standard mass-flow

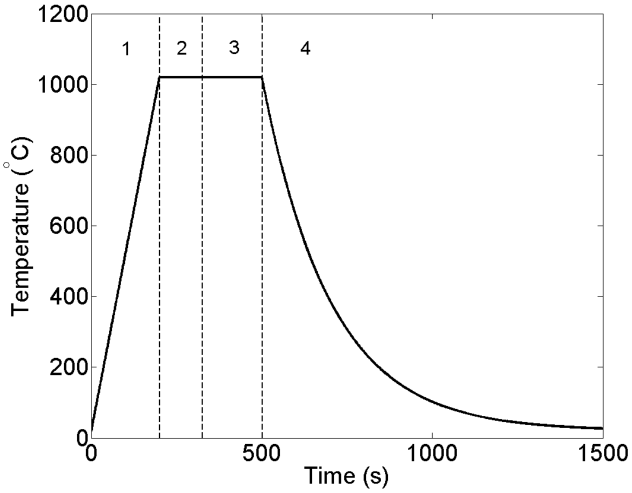

Figure 7: Temperature profile divided into steps for a typical graphene CVD process. Heating up (1), annealing at constant temperature (2), growth (3) and cooling down (4).

controllers. So, CH_4 diluted in Ar (5%) is used as a precursor gas mixture. Also, argon introduces a diffusion barrier for CH_4 and H_2, which provides additional control on the rate of decomposition of CH_4. Hydrogen has several roles in this process [52]. Its main role is to etch away the carbon atoms which are not connected to the already grown graphene, thereby decreasing the number of nucleation centers. The way the pressure and the gas flows influence the graphene growth can be understood from Le Chatelier's principle and Eq. 13. High methane partial pressure, low hydrogen partial pressure and low overall pressure give high carbon deposition rate and high nucleation density (ND). That is why for fast growth of continuous graphene films, low pressure and high methane flow were used [11, 53]; and for slow growth of large graphene single crystals (low ND) low methane flow and atmospheric pressure were used [54, 55].

The role of temperature turns out to be more complicated. From Le Chatelier's principle, a higher temperature should speed up the forward reaction rate and therefore give faster graphene growth. On the other hand, according to thermodynamics, higher temperature decreases the ND slowing down the formation of graphene [56]. We summarized the influence of these parameters on the growth results in Fig. 8.

There are two main types of CVD systems for graphene: hotwall and coldwall. In a hotwall system an external heater is used to heat up the whole growth chamber. Since the walls are heated together with the sample, this

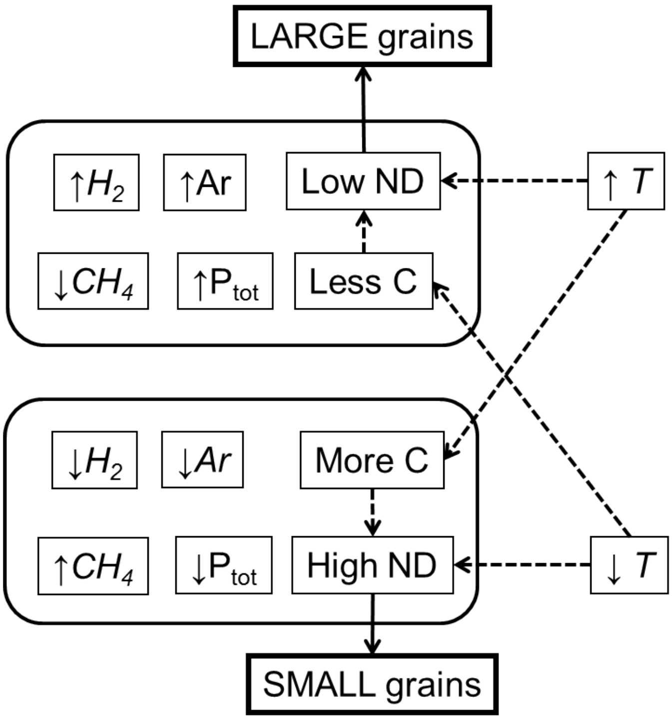

Figure 8: The main parameters of CVD graphene process and how they influence the growth. High nucleation density (ND) gives small grains and is used for fast growth of continuous graphene film [57]. Low ND gives large grains and is used to grow standalone graphene monocrystals [58]. Adopted from Paper **I**.

allows for stable and uniform heating of both the sample and the surrounding gases. In a coldwall system, the heater is used to heat up only the sample. Both types have their pros and cons. The temperature distribution inside a hotwall system is usually much more uniform than in a coldwall one. On the other hand, the time required for a hotwall system to reach 1000°C is typically 1-2 h and even more to cool down. The graphene growth process in a coldwall system can be as fast as 30 mins from loading to unloading the sample due to the small heated volume.

We introduced a combined design of graphene CVD system (see Fig. 9) by adding one more heater in parallel to the existing one. The sample was placed in between the heaters and supported by ceramic spacers. The two heaters and the spacers had a small volume of $\sim$1000 mm^3. The sample was surrounded by heaters; this arrangement resembled a hotwall chamber. The temperature distribution within this small "hotwall" chamber was much more uniform than in the original design with only one heater. In Chapter

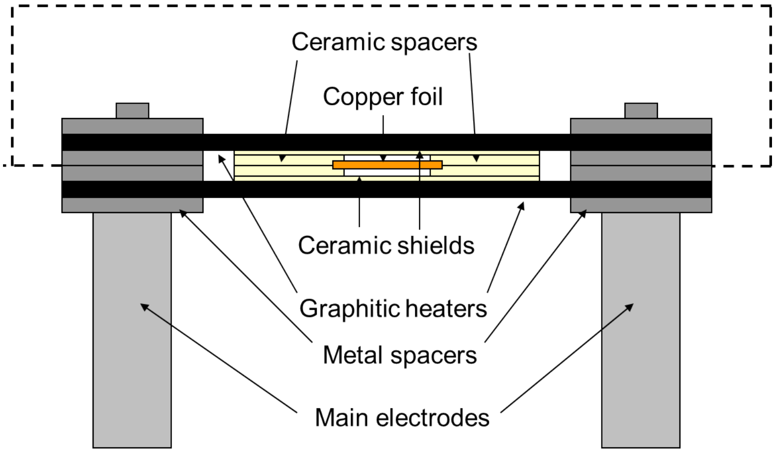

Figure 9: The side view our hybrid-type setup. The dotted line indicates the added parts. Adopted from Paper **I**.

6 we present and discuss simulation results for both setups to support this statement. According to the simulations, the temperature of the sample in the hybrid-type system is indeed more uniform and closer to the temperature of the heaters. This gives a better control over the temperature of the sample.

As mentioned above, graphene is mostly grown on metals. Although, it is possible to grow graphene without a metal catalyst, its quality in this case is relatively low [59]. When graphene is grown on metals, it needs to be transferred to an insulating substrate. Since graphene is an atomically thin material, vulnerable to macro-scale forces, transferring appears to be quite a challenging task. One should somehow protect the graphene film and provide it with support when detaching from the metal and applying to the target substrate. The most common way is to cover graphene with a polymer called Polymethylmethacrylate (PMMA). This provides a flexible mechanical support for graphene once the metal is removed. After the transfer, this polymer can be dissolved in acetone. There are mainly two ways to release the grown graphene from the metal substrate: to etch the substrate away by chemicals or to detach it mechanically. Etching was first implemented for Ni substrates [51], but is also possible for copper [60]. Metals like platinum, ruthenium or iridium are very expensive; they also require mixtures of strong acids to etch, therefore graphene grown on them is usually mechanically detached. One of the ways is to perform an electrolysis and use the gas bubbles to separate graphene from the metal [61].

We compared the growth of graphene in the original cold-wall setup and in the upgraded hybrid-type setup. First, we tried to achieve the lowest ND for each setup and compare. We terminated the growths before the first

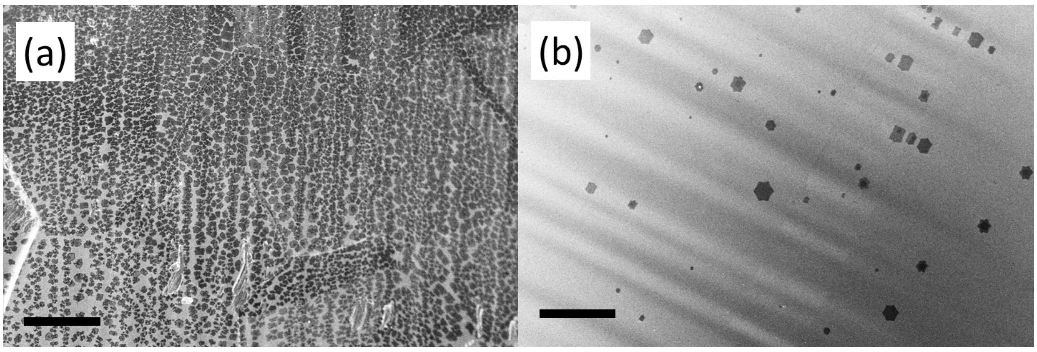

Figure 10: SEM images of graphene crystals grown in the original (a) and converted (b) setups. The growth was terminated before completion of the first graphene layer. The scale bars are 50 μm.

graphene layer was complete, for the graphene crystals to be visible in the scanning electron microscope (SEM). In Fig. 10 we present SEM images of graphene crystals nucleated in both setups. We see that due to the increased temperature stability and uniformity, it is possible to substantially decrease ND and improve the quality of graphene. For subsequent analysis we grew continuous films in both setups as well as single crystals in the converted setup. The graphene was transferred from copper to SiO_2/Si chips using the common etching method for some of the samples, or the bubbling transfer technique for the others. The transfer recipes used for this are presented in Appendix: Methods and Recipes.

We used Raman spectroscopy to initially characterize the transferred graphene. This method allows to gain initial information of graphene quality without fabricating a device [48]. In Fig. 11, we present Raman spectra for the continuous graphene films grown in both setups. After normalizing them by the amplitude of the G peak we calculated the peaks amplitude ratios. For the graphene grown in the original setup, the ratios were: D:G = 0.3, G:2D = 0.45; whereas for the graphene grown in the new setup: D:G = 0.2, G:2D = 0.26. Low D peak and high 2D peak relative to the G peak show lower defect concentration (i.e. higher quality of the graphene [62]). This was the initial quality comparison, which indicated a higher quality of the graphene grown in the new double-heater setup. After that, we fabricated standard Hallbar devices out of the transferred graphene. The typical room temperature carrier mobility in the graphene grown in the original setup was ~ 2000 cm^2/(V s), for the converted setup - ~ 4000 cm^2/(V s). We explain this difference in mobilities by larger grains in the latter case: there were less grain boundaries within the device, which are scattering centres for the charge-carriers.

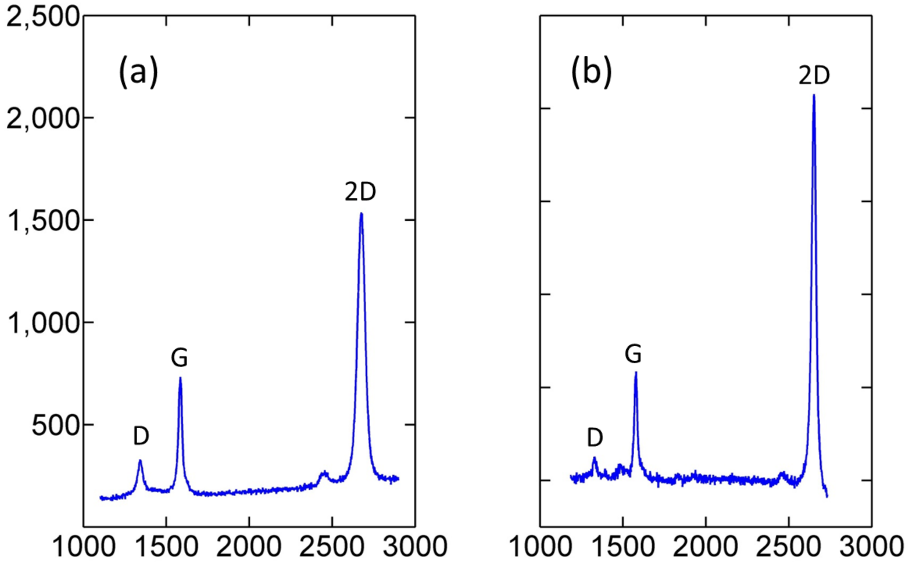

Figure 11: Typical Raman spectra for continuous graphene films grown in the original (a) and converted (b) setups. The D peak in (a) is higher than in (b) and the 2D peak in (a) is lower than in (b) indicating the difference in graphene quality. The laser wavelength is 638 nm. Adopted from Paper **I**.

To summarize, we showed that it is important to have good control over growth parameters for graphene CVD process. This is particularly difficult for cold-wall CVD systems due to high temperature gradients close to the sample. We demonstrated a conversion of the originally cold-wall setup into a hybrid-type one, where we achieved a better temperature control. We characterized the quality of graphene and showed its improvement after the conversion. We also carried out computer simulations of the heaters for both setups to visualize the temperature distributions (see Chapter 6).

4 Graphene encapsulation

First graphene devices were fabricated on SiO_2/Si substrates [63]. The top surface of graphene was open to ambient and therefore - to contaminants. Moreover, during the device fabrication process, i. e. lithography, the graphene was in contact with different chemicals, which left residues even after cleaning. Since graphene is sensitive to doping, these contaminants can shift the Dirac point and significantly change the device resistance. Moreover, the open top surface can attract additional contaminants over time, making the device resistance unstable. To solve this problem, graphene can be covered and thus protected from the environment before the fabrication process to preserve its properties and make the devices more stable.

4.1 Graphene-hBN heterostructures

Graphene is not the only 2D material known for interesting properties. Hexagonal boron nitride (hBN) and some transition metal dichalcogenides are also 2D materials [64]. If combined with graphene and/or with each other, the resulting heterostructures can show even more new effects [65]. In fact, hBN is the best known substrate for graphene [28].

Boron nitride exists is several allotropic forms: α-BN (hexagonal), β-BN (cubic), w-BN (wurtzite) and other more rare ones. The first one, hexagonal, is of particular interest, since in this form BN resembles the hexagonal graphite lattice with a similar layered structure. It is even called ”white graphite” for its similarity to graphite.

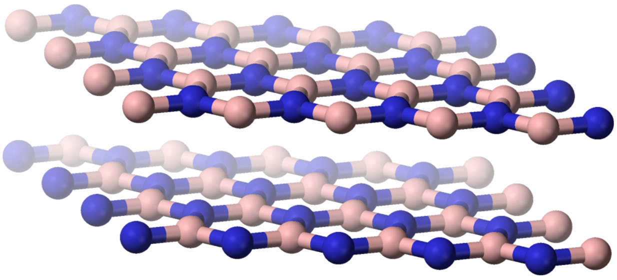

Figure 12: Illustration of hBN layers. Blue and beige spheres correspond to boron and nitrogen atoms, respectively. The picture is taken from https://commons.wikimedia.org/wiki/File:Boron-nitride-(hexagonal)-side-3D-balls.png (free license).

The main difference from graphite is the large bandgap about 5 eV in hBN, which makes it a good insulator. It is also temperature- and chemically stable, reacting only with molten bases at high temperatures. All these properties allow hBN to be very useful for applications in combination with graphene.

Due to a strong Van-der-Waals interaction between graphene and hBN, these materials can form heterostructures, where for example graphene is intercalated between hBN layers [65]. In this case graphene is securely protected and can show its intrinsic properties unaffected by the environment.

However, there are lots of challenges in the experimental realization of these heterostructures. First of all, hBN, contrary to graphite, is not found in nature. The crystals of hBN are artificially grown and by now the high quality and purity are achieved only in one lab [66]. These crystals can be cleaved with a sticky tape the same way as graphite to produce several nm thin and even monolayer flakes. The technology of assembling hBN-graphene-hBN sandwiches is now well known [67, 68]. Typical steps of this process are presented in Fig. 13.

First of all, graphene- and hBN flakes are obtained by exfoliation on SiO_2/Si substrates (see Chapter 3). A gel-like polymer Polydimethylsiloxane (PDMS) attached to a glass slide is used as a transparent soft "cushion" to pick up- and transfer flakes. The glass slide is mounted on a micropositional stage, which allows movements along three axes with a micron precision. The bottom surface of the PDMS is covered by Polypropylene Carbonate (PPC) which has low glass-transition- and melting temperatures ($25 - 40°C$ and $80 - 90°C$, respectively). It is possible to control the adhesion of other materials to this polymer by changing the temperature, which is achievable by using a small several-Watt local heater. To pick up an hBN flake from SiO_2 surface, the PDMS unit is aligned over the flake and carefully brought in contact with its surface (see Fig. 13 step I). The PDMS is soft; it assumes the flat shape of the SiO_2 surface and compensates for a possible tilt. After that, the substrate is heated to $40°$ to soften the PPC layer and make it assume the microscale shape of the flake. Then, the glass slide with PDMS is slowly removed from the surface lifting up the flake.

To transfer the flake to another substrate, it is first moved to the target position and then slowly pushed to the surface. Then, the PPC is heated up to its melting point ($90°$), which makes it loose the contact with the flake and leave it on the surface at the desired position. For a graphene flake, the pick up process is slightly different. It is difficult to pick it up just with PPC/PDMS, but it can be picked up with a hBN flake, already attached to the bottom of the PPC layer [67], using the strong van der Waals interaction between hBN and graphene [65]. So, the process of assembling a full hBN-graphene-hBN sandwich occurs from top to bottom: the top hBN flake

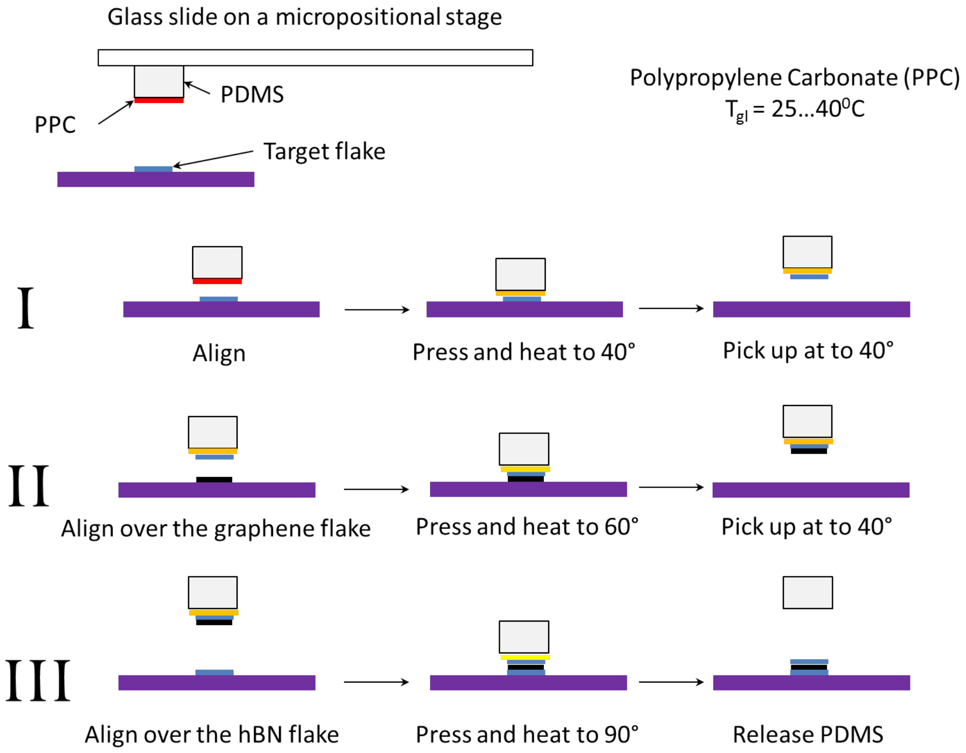

Figure 13: The steps of dry assembling of a hBN-graphene-hBN sandwich. Picking up a hBN flake (I) with PPC on PDMS, picking up a graphene flake with the hBN flake (II) and transferring them both on top of another hBN flake (III).

is picked up first, then it picks up the graphene and finally hBN-graphene stack is placed on the bottom hBN flake and released (see Fig. 13). It is important to emphasize that during the whole process the graphene flake is not in contact with anything except SiO_2 and hBN; this drastically reduces the amount of contaminants. It is also called "dry transfer" method. Those few contaminations, which still appear between graphene and hBN, are pushed together by the strong Van-der-Waals interaction between graphene and hBN leaving some areas completely clean [65]. The already assembled hBN-graphene-hBN heterostructures can also be annealed under vacuum at high temperature ($500 - 600°C$) in order to provoke contaminations movement and their further coagulation. In Fig. 14, optical images of such a heterostructure (a) and devices fabricated from it (b) are presented.

This particular heterostructure was assembled using a commercially available hBN. We used vacuum annealing to get rid of the impurities. Images from atomic-force microscope (AFM) before- and after the annealing are presented in Fig. 14c and Fig. 14d, respectively. We see that many impurity bulbs disappear, leaving some areas completely clean. These areas are big enough to place μm-large devices. Previous studies indicated that these bubbles consist mostly of hydrocarbons [69]. This agrees with the results on air contamination investigation [70], which shows maximum particle concentration in the air for 200 nm size and hydrocarbons as the most abundant compounds in those particles. Even in the cleanroom environment, which is used to assemble heterostructures, there is still some amount of particles in the air, which are not stopped by filters. The only way to avoid these particles seems to be using glovebox ventilated with a pure inert gas (argon or nitrogen).

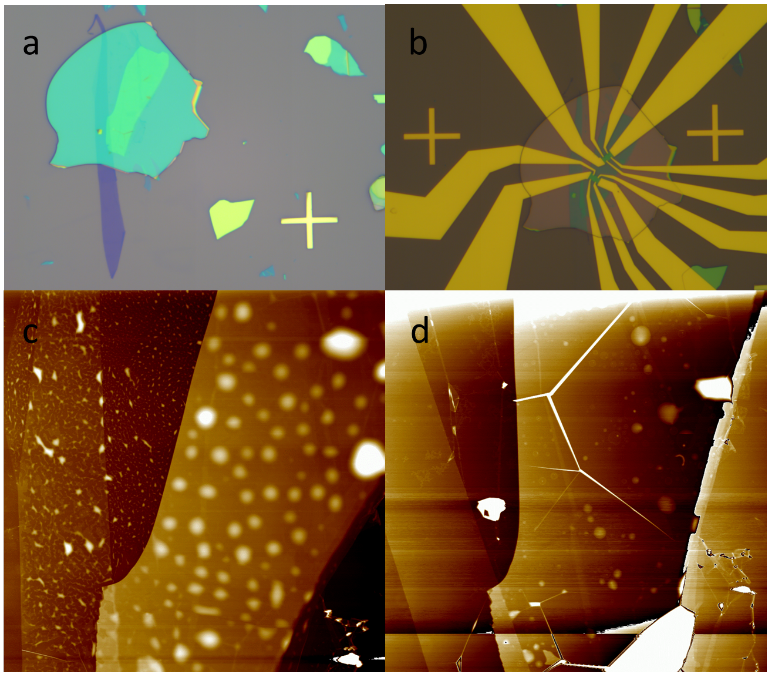

Figure 14: (a) Optical image of an assembled hBN-graphene-hBN heterostructure. (b) Optical image of the same heterostructure after device fabrication. The size of the crosses is 20 μm. (c,d) 20×20 μm^2 AFM images of the same heterostructure before and after vacuum annealing respectively. The bulbs of impurities almost disappear leaving some areas clean and flat.

Another interesting topic to discuss is how to make electrical contacts to these devices. It is impossible to make conventional surface contacts to graphene encapsulated in hBN. There is no way to selectively etch hBN from top of graphene. Of course, graphene flake can be chosen bigger than the

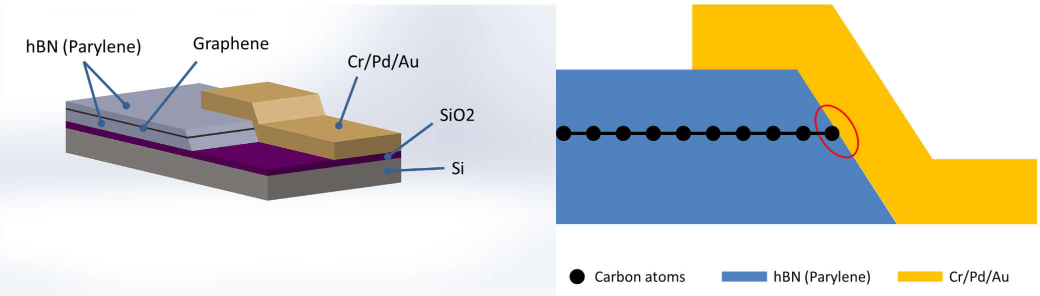

Figure 15: An illustration of encapsulated graphene and 1D edge contact to it (highlighted with red oval).

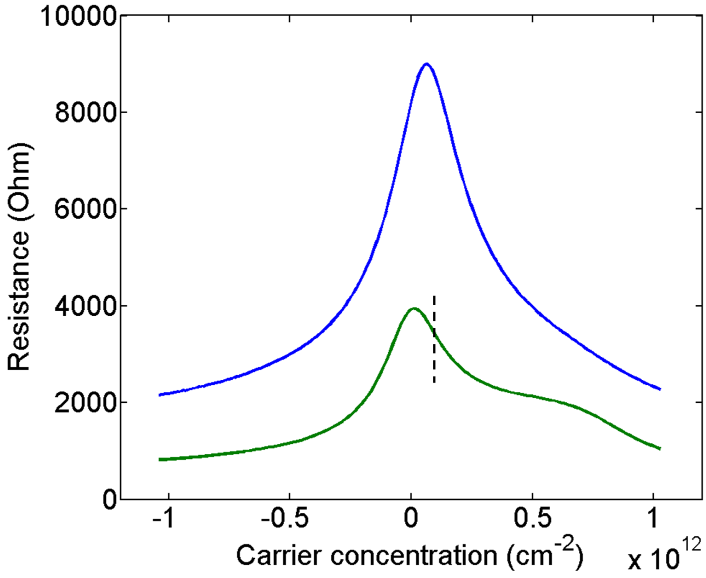

Figure 16: The two-probe resistance vs carrier concentration for two hBN-encapsulated graphene devices. Fitting to Eq. 3 gave the following parameters: $\mu = 14000$ cm^2/(V s), $n_0 = 1.4 \times 10^{11}$ cm^{-2} for the blue curve and $\mu = 42000$ cm^2/(V s), $n_0 = 1.0 \times 10^{11}$ cm^{-2} for the green curve. Since the green curve is asymmetric, the fitting was done only for the part of the curve to the left of the dashed line.

top hBN and therefore can be contacted via those uncovered regions [20], but it adds more difficulties such as limited choice of flakes and complicated alignment of them.

One-dimensional (1D) edge contacts were suggested and successfully implemented previously [50]. When the hBN-graphene-hBN structure is sliced by plasma etching during the lithography process, the resulting 1D row of carbon atoms faces the ambient and can be metallized. These purely 1D metal-to-graphene contacts show very low line resistivity $\sim 100\ \Omega \cdot \mu\mathrm{m}$. A schematic view of such a contact is presented in Fig. 15. The slope of the slice is achieved due to the finite etch rate of the resist mask used during the lithography.

For the devices presented in Fig. 14(b), we measured the transfer curves (see Fig. 16). The extracted mobilities were $\mu_1 = 14000\ \mathrm{cm}^2/(\mathrm{V\ s})$ and $\mu_2 = 42000\ \mathrm{cm}^2/(\mathrm{V\ s})$; the residual carrier concentrations $n_{01} = 1.4 \times 10^{11}\ \mathrm{cm}^{-2}$ and $n_{02} = 1.0 \times 10^{11}\ \mathrm{cm}^{-2}$. We also saw that the Dirac point was close to zero. Although the device quality was high, it was yet an order of magnitude lower than that of the state-of-the-art devices [50, 68]. We attribute this to the poor quality of the hBN used and possibly - not enough cleaning of the fabricated hBN-graphene-hBN structures. Only after these experiments we became aware of the idea of mechanical cleaning of such structures [71]. Moreover, our samples were of relatively small size ($2 \times 5\ \mu\mathrm{m}^2$), therefore very vulnerable to static discharges. Unfortunately, they did not survive until the low-temperature measurements.

To summarize, hBN-graphene-hBN heterostructures are hand-made one by one, which is a time-consuming process. The shapes and thicknesses of hBN flakes are random making each device unique. And finally, the lateral size of these heterostructures is limited to $\sim 100\ \mu\mathrm{m}$ which makes it impractical to fabricate wafer-scale arrays of devices. Recent progress in the quality of CVD-grown hBN is promising [72], but still far from that of the exfoliated flakes. This motivated us to look for a replacement for hBN. As such a replacement we used a polymer called Parylene.

4.2 Encapsulation of graphene in Parylene

Parylene is a well known material in industry; it is primarily used as a protecting layer for microcircuits [73]. The chemical formula of Parylene and some of its derivatives are presented in Fig. 17. The particular interest in Parylene comes because of the combination of the following properties [74]. Thin layers of Parylene can be deposited at room temperature. It provides a conformal coverage. It is hydrophobic. Its dielectric constant is close to that of $\mathrm{SiO_2}$. Parylene is not solvable in any solvents and is stable up to 400°C. All this makes it a very valuable candidate as a replacement of hBN in graphene heterostructures.

An example of a Parylene deposition machine is depicted in Fig. 18. The precursor for Parylene deposition is a Parylene dimer of certain type (N, C, D, HT or other). These dimers have the sublimation temperature

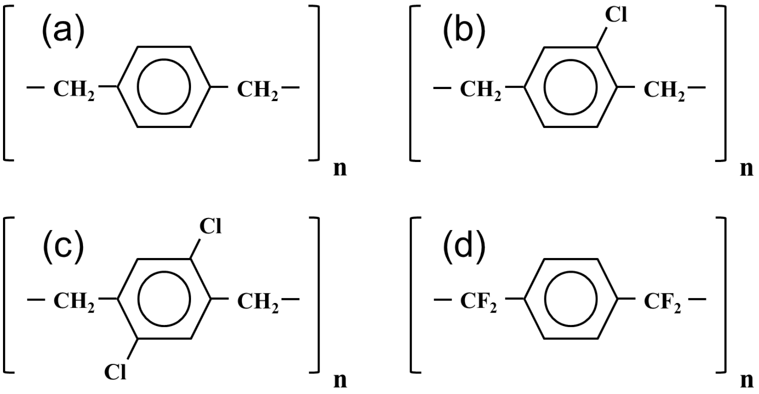

Figure 17: Chemical formulas of Parylene N (a) and its derivatives: Parylene C (b), Parylene D (c), Parylene HT (d).

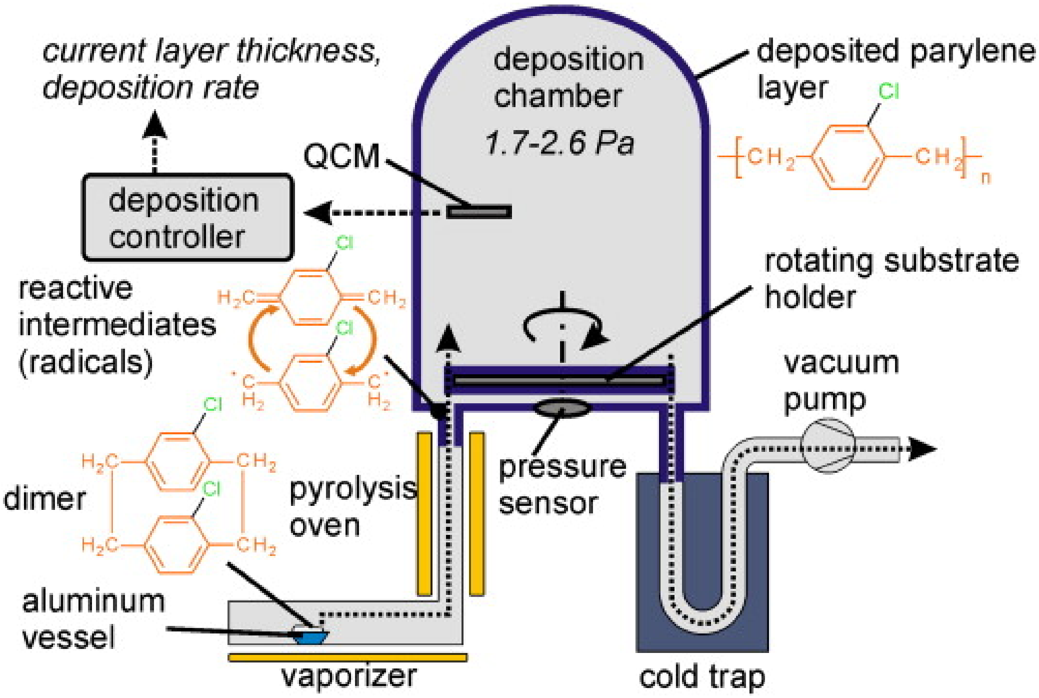

Figure 18: A Parylene deposition machine. Adopted from [75] with permission. (©Thin Solid Films).

160 – 180°C. First, the system is pumped down to forevacuum (1 mbar), the dimer is heated up to this temperature and thus evaporated. Then, the dimer vapour flows through a hot furnace (650 – 690°C) and breaks down to monomer. Finally, the active monomer radicals enter the deposition chamber

and cover everything including the samples. The deposition chamber and the samples are at room temperature during the deposition. The final thickness of Parylene is defined by the mass of the dimer loaded into the system.

The idea of protecting graphene devices with Parylene from one side was implemented previously for graphene on SiO_2 [76]. However, when the substrate is SiO_2/Si, which is highly hydrophilic, the device still gets all the drawbacks like lower mobility and extra doping [77]. In our case, the graphene was protected with hydrophobic Parylene from both top and bottom and had no contact with SiO_2. We used two types of Parylene available in our lab, N and C. We started with a SiO_2/Si substrate, where SiO_2 layer was 90 nm thick and deposited 150 nm of Parylene N (or 155 nm of Parylene C) on top. The resulting Parylene/SiO_2/Si stack was similar to the standard 290 nm SiO_2/Si: it provided a similar contrast to the graphene flakes exfoliated on it. The exfoliation method was the same as the one used for the ordinary graphene samples on SiO_2/Si chips (see Chapter 3). We also measured the surface roughness of deposited Parylene and compared it with that of SiO_2. We present this comparison in Fig. 19. The roughness of deposited Parylenes appeared to be almost an order of magnitude higher than for SiO_2.

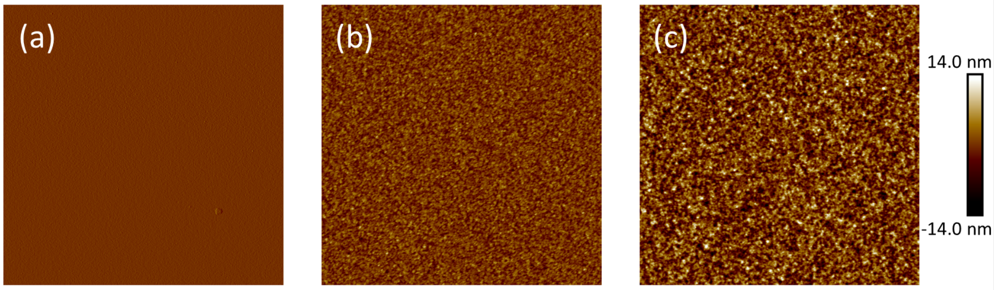

Figure 19: The tapping mode AFM scans of SiO_2 (a), Parylene N (b) and Parylene C (c). The corresponding roughnesses are 0.27 nm, 2.0 nm and 4.0 nm. The size of the scans is 10×10 μm^2 each. Adopted from Paper **II**.

The exfoliated graphene was immediately covered by another layer of Parylene to finalize the encapsulation and to minimize the sample contamination. Even after the deposition of the top layer of Parylene, the contrast of graphene was still sufficient for seeing the flakes in the optical microscope. Optical images of monolayer graphene flake before- and after the top Parylene layer deposition are presented in Fig. 20.

To characterize the encapsulated graphene, we fabricated Hallbar devices. The device fabrication consisted of two lithography steps: defining the device geometry and electrode deposition. The etching of the device shape is done in

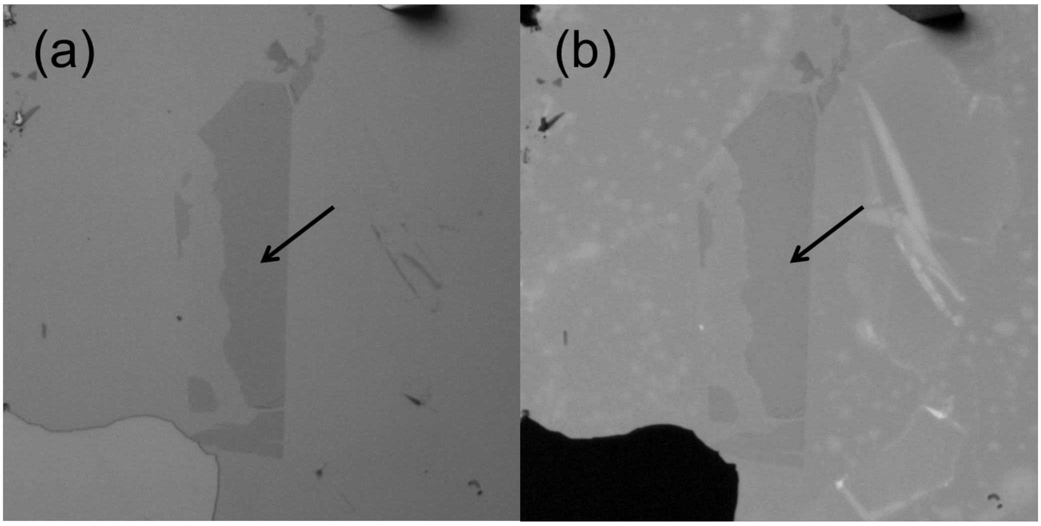

Figure 20: Optical images of graphene on Parylene. (a) Graphene on Parylene (150 nm)/SiO_2 (90 nm)/Si. (b) Parylene (90 nm)/ graphene /Parylene (150 nm)/SiO_2 (90 nm)/Si. Both images have good optical contrast sufficient for doing lithography. Adopted from Paper **II**.

O_2-plasma. The SiO_2 layer prevents any electrical contact between the electrodes and Si. The electrodes consist of Cr (1 nm)/Pd (15 nm)/Au (200nm) thin films and form a 1D edge contact to graphene. More details about the fabrication recipes are available in Appendix: Methods and Recipes. An example of a Hallbar device fabricated from an encapsulated graphene flake is presented in the inset of Fig. 21.

The most common and universal parameter to characterize the quality of graphene device is the charge-carrier mobility. We deduced it in two ways: from the fitting of the field-effect curve and from the Hall effect (see Chapter 2). For the first method, we measured the two-probe resistance of the device channel (contacts 1 and 5 in the inset of Fig. 21) vs the back-gate voltage. These measurements were performed at room temperature directly in the cleanroom after the sample fabrication. Results for several samples are presented in Fig. 21. They show only small shift of Dirac point. We explain this by the chemical inertness of Parylene N, its hydrophobicity, and absence of strong electron donors or acceptors in its chemical formula. Contrary to Parylene N, Parylene C shows a significant doping caused in our opinion by the chlorine atom in the chemical formula. The extracted values of the carrier mobility are in the range $5000 - 7000$ $cm^2/(V\ s)$, which is common for graphene on SiO_2 but lower than for graphene on hBN. We explain this by a significant surface roughness of Parylene which possibly creates inhomogeneity and adds scattering centres for charge-carriers. The average value of residual carrier concentration was $n_0 = 3.0 \times 10^{11}$ cm^{-2} in this case. The average contact resistance was $\sim 50\ \Omega$ per contact.

We also tried annealing (3 h at 200°C in N_2) as a way to clean samples and possibly increase the mobility. Unfortunately, annealing of ready devices increased the contact resistance to $R_c \sim 100$ kΩ, which made further electrical measurements impossible. But when unpatterned graphene was annealed and lithography was done, the resulting devices performed well ($\mu = 8000 - 10000$ cm^2/(V s)) and the average contact resistance was as previous - $\sim 50\ \Omega$ per contact (see Fig. 21). The mobility of the annealed samples was higher than that without annealing, but we saw also some shift of the Dirac point ($\sim 0.7 \times 10^{12}$ cm^{-2}). Since it was impossible to compare the same device before and after annealing, we cannot draw any conclusions on the effect of annealing. One of the later encapsulated samples showed the room-temperature mobility $\mu = 30000$ cm^2/(V s), without being annealed. That sample is discussed in Chapter 5.

We derived the mobility from the Hall effect in low magnetic field, where the transverse resistance is linear with the magnetic field (see Eq. 8) and obtained the values close to those from fitting the transfer curves. At high magnetic field (up to 12 T) we observed the Quantum Hall effect (QHE). It is presented as a false-color 3D plot of the device resistance versus magnetic field and charge-carrier concentration. The latter was controlled by the back gate voltage. Such a plot for one of the samples is presented in Fig. 22. It is also called "fan-diagram" and has well-defined plateaus of zero resistance, some of them visible in relatively low magnetic fields (around 3 T). These plateaus correspond to the filling factors $\nu = \pm 2, \pm 6, \pm 10 \ldots$.

These zero-resistance plateaus allow to measure the contact resistance directly. The contact resistance can be deduced from the three-probe measurements in QHE state when the longitudinal resistance of graphene is zero ($T = 2K, B = 8T$). For example, if we want to measure the resistance of contact 3 in the inset of Fig. 21, we send current between contacts 2 and 3 and measure voltage between contacts 3 and 4. This measurement returned the resistance of the graphene-metal contact plus the resistance of the electrode itself. We estimated the latter to be $\sim 0.3\ \Omega$, and neglected it. The lowest measured value during this three-probe experiment was $R_c = 2.1 \pm 0.5\ \Omega$ with the graphene-metal contact length $l = 7\ \mu$m. This corresponds to 1D contact resistivity of around 14 $\Omega \cdot \mu$m, which is even lower than that reported for hBN-graphene heterostructures [50].

We also tested the possibility to scale up this technology and fabricated large-scale encapsulated devices of CVD graphene. The steps of encapsulating CVD graphene are presented in Fig. 23. We started from conventional

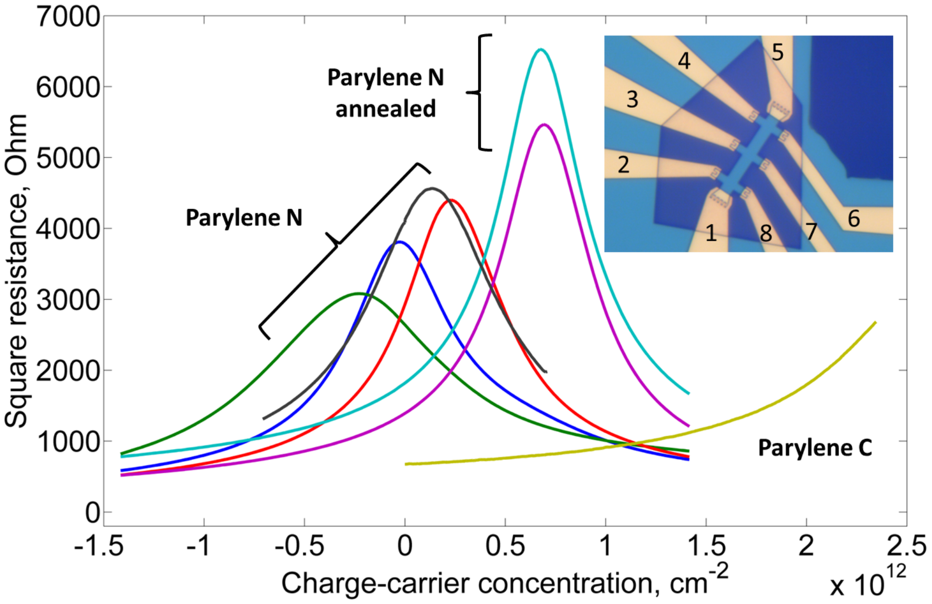

Figure 21: Transfer curves for the devices fabricated from graphene encapsulated in Parylene. For the samples with Parylene N, we see that the Dirac point is close to zero and they show room temperature mobilities in the range 5000 - 7000 cm^2/(V s). For the sample with Parylene C, the Dirac point lies far from zero. The annealed samples show a higher mobility (8000 - 10000 cm^2/(V s)), but also slight additional doping ($\sim 7 \times 10^{11}$ cm^{-2}). The charge concentration 10^{12} cm^{-2} corresponds to the back-gate voltage $V_g = 14.3$ V. An optical image of one of the devices is presented in the inset. The scale bar in the inset is 10 μm. Adopted from Paper **II**.

CVD graphene grown on copper foil. First, we covered the sample with Parylene. Then we glued it to SiO_2/Si chip with copper facing up. After that, we etched away the Parylene deposited on copper in O_2-plasma and then etched away the copper in $(NH_4)_2SO_4$ solution. After etching, the sample was rinsed in DI water, blow-dried and covered with another layer of Parylene, which finally encapsulated the graphene. We fabricated Hallbar devices from this graphene in order to further characterize this method of encapsulation and to test the possibility of making edge-contacts. General photolithography was used to pattern the devices and to fabricate the metal electrodes (see Appendix: Methods and Recipes for details). In total, we fabricated 72 hallbars, half with Parylene N and Parylene C. The samples with Parylene C had cracks, which partially destroyed some of the devices; all the Parylene N devices were fully functional except for one. An optical image is presented in

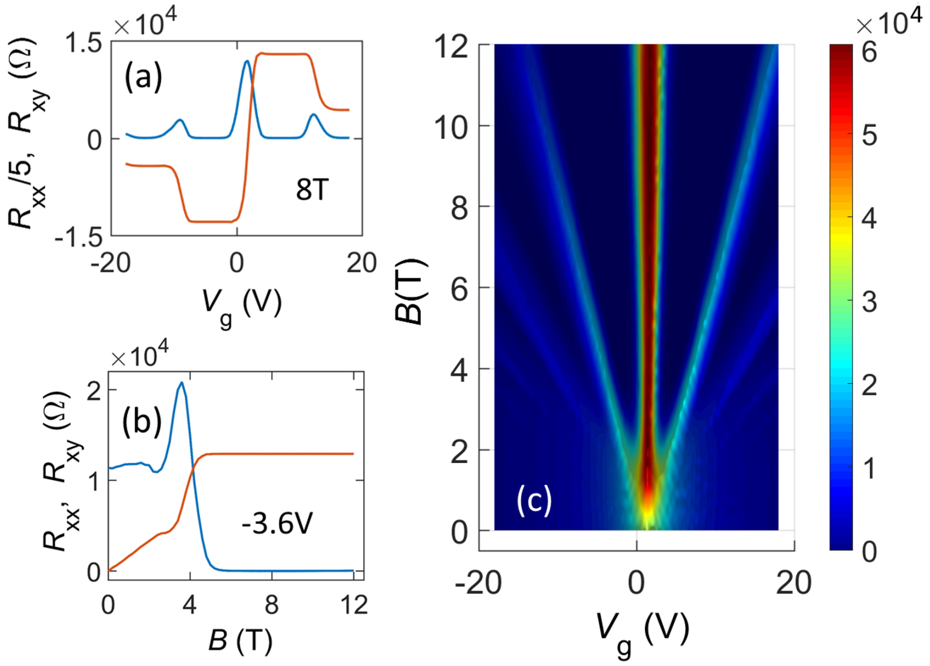

Figure 22: Quantum Hall effect in encapsulated graphene device at $T = 2$ K. (a) The longitudinal(R_{xx}, blue) and Hall(R_{xy}, red) resistances as functions of the back-gate voltage V_g at $B = 8$ T. (b) R_{xx} (blue) and R_{xy} (red) as functions of B at $V_g = -3.6$ V. (c) A false-color 3D plot of $R_{xx}(V_g, B)$. We see well-defined Hall plateaus starting from $B = 3$ T. $V_g = 1$ V corresponds to charge density change 7.0×10^{10} cm^{-2}. Adopted from Paper **II**.

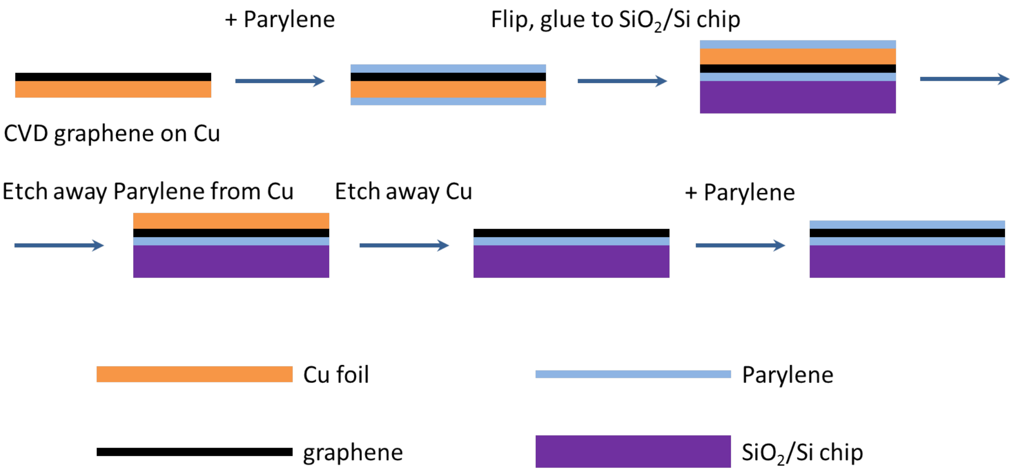

Figure 23: The steps of the encapsulation process of CVD graphene.

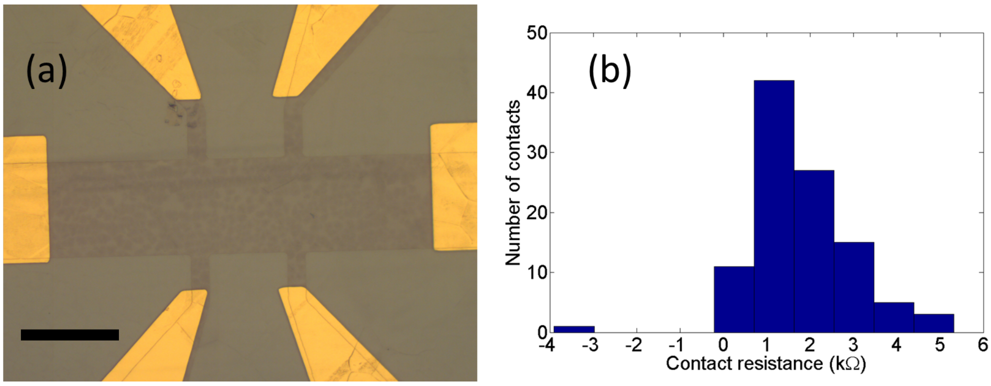

Figure 24: (a) A large-scale Hallbar device fabricated of CVD graphene encapsulated in Parylene N. The device showed mobility $\mu = 1000$ cm^2/(V s) both at 300 K and 2 K. The Dirac point was not reachable within ±30 V applied to the back-gate. Th scalebar is 100 μm. (b) Statistics of contact resistances for these devices based on 214 contacts.

Fig. 24. A brief quality check showed that the devices had temperature independent mobility about $\mu = 1000$ cm^2/(V s). The Dirac point was shifted by more than 30 V of equivalent gate voltage for the two samples with top gates. For all functional contacts we estimated their contact resistance using the three-probe measurement method. Since the samples did not show QHE, it was not possible to "nullify" the resistance of the graphene parts, which contributed to the three-probe measurements. Moreover, due to a slight misalignment of the two lithography layers, the length of each part was different for every contact. So, we measured those lengths from the optical images and subtracted the estimated resistance from the three-probe measurements. Finally, we got statistics of the estimated contact resistances for all working contacts. The average contact resistance was 1.2 kΩ corresponding to line resistivity 760 k$\Omega \cdot \mu$m. This value is substantially higher than the contact resistivity for exfoliated devices. We explain this by possible contamination of the graphene edge by the photoresist that we used (see Appendix: Methods and Recipes).

In summary of this chapter, we can conclude that encapsulating graphene has many benefits in terms of the resulting device performance. We introduced a replacement of hBN, Parylene, which makes graphene encapsulation potentially scalable and provides high mobility devices suitable for some applications. The experiments with encapsulated CVD graphene show the possibility to fabricate large-scale encapsulated devices with edge-contacts.

5 Graphene bolometers

5.1 Introduction

Devices that convert radiation (photons) to electric signal have always been on high demand for various applications, especially for high frequencies. There are many types of high frequency radiation detectors, for example: Schottky diodes [78], field-effect detectors [79], superconducting transition-edge sensors [80], cold-electron bolometers [81] and hot-electron bolometers [82]. The graphene-based hot-electron bolometers are of our particular interest within the scope of this thesis. The previously reported graphene radiation detectors are based on the field-effect [83] or on the photovoltaic (PV) and thermoelectric (TE) effects [84, 85, 86, 87].

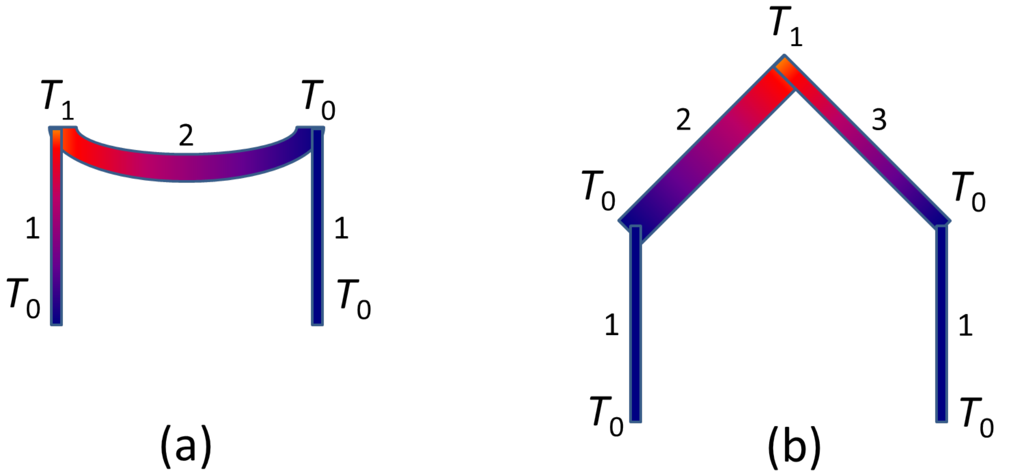

Figure 25: Illustration of a conventional thermocouple (a) and a more advanced one (b), which was realized in this work. The numbers indicate different materials, the color fill indicates different temperature.

Thermoelectric effects can be measured experimentally in thermocouples created by connecting two or more materials with different S (see Fig. 25). Thermoelectric voltage appears if there is a temperature difference between the thermocouple joints and is expressed as: $V_{TEP} = \int S(T)dT$. Unfortunately, a graphene-metal thermocouple appears to be inefficient, due to the fact that the electrons in graphene are efficienly cooled down by those of the metal [88]. Alternatively, an intrinsic graphene thermocouple, created by connected areas with different S, appears to be much more efficient. It can be realized in a dual-gated design [84], which allows for the hottest region in graphene (the hotspot) to be located at- or close to the junction, maximizing the readout voltage.

5.2 DC thermoelectric graphene device

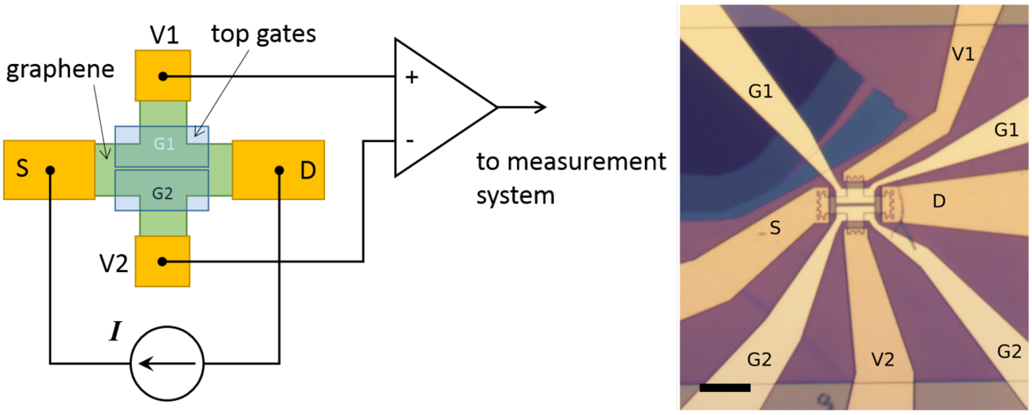

Figure 26: A principle scheme and an optical image of DC thermoelectric device. Current runs from source (S) to drain (D), heating up the $p-n$ junction. Thermoelectric voltage appears between the electrodes V1 and V2. The scalebar is 10 μm. Adopted from Paper **III**.

All our thermoelectric devices benefited from the Parylene encapsulation technology (see Chapter 4). The first type of thermoelectric device which we studied is presented in Fig. 26. The device was cross-shaped with four contacts to it and was also equipped with two top gates and bottom gate. The areas overlapped with the top gates formed an intrinsic graphene thermocouple, with the Seebeck coefficients defined by the voltages applied to them. The heating of the device was done by simply running DC current from the source (S) to drain (D) contacts. Due to the raise of electronic temperature in the junction, the thermoelectric voltage V_{TEP} occurred between the contacts V1 and V2, which were transverse to the current direction thus excluding the longitudinal component of the signal. V_{TEP} is a function of four parameters I, V_{bg}, V_{tg1}, V_{tg2}. Here I is the DC source-drain current, V_{bg} is the back-gate voltage, V_{tg1} and V_{tg2} are the top-gate voltages. In Fig. 27 we present the plot of $V_{TEP}(I, V_{bg})$ with other two parameters fixed at $V_{tg1} = -V_{tg2} = 1$ V. We saw strong signal up to 40 mV, which corresponded to DC responsivity of the device around 90 V/W. The signal V_{TEP} was positive for both signs of the DC current I (see Fig. 27), which clearly proved the thermoelectric nature of the signal. We expected the $V_{TEP}(I)$ function to be even, since the Joule heating is proportional to I^2. However, we see that the two maxima of

V_{TEP} are shifted relative to each other along the V_{bg}-axis. We explain this by the self-gating effect, which is strong at high electrical currents in graphene. To support our explanation we performed computer simulations including this effect and see a good qualitative agreement with the experimental plot (see Fig. 37(b) in Chapter 6).

The high responsivity and simplicity of the device design suggested fabrication of a radiation detector. Indeed, the heating of electron system can be done by the power received by antenna attached to the S and D contacts, forming in this case a thermoelectric graphene bolometer.

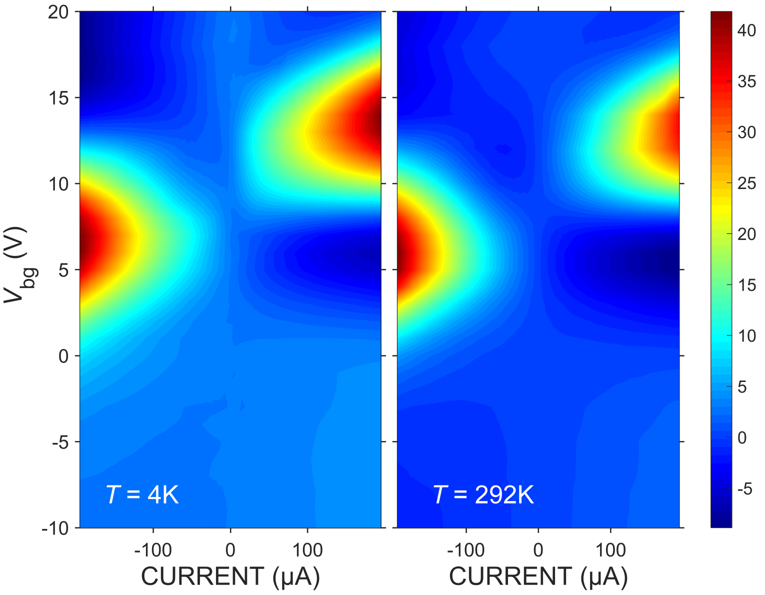

Figure 27: False-color plots of TEP signal as a function of the back-gate voltage V_{bg} and the bias current I. The voltages applied to the top-gates are $V_{tg1} = -V_{tg2} = 1$ V. The maximum achieved TEP signal is higher than 40 mV, which corresponds to responsivity ~ 90 V/W. The color scale is in mV. Adopted from Paper **III**.

5.3 Thermoelectric graphene bolometers

A prototype thermoelectric graphene bolometer is presented in Fig. 28. The design resembled the previously fabricated DC thermoelectric device with the S and D contacts replaced with an antenna; the other contacts had the same functionality as before. They were made very narrow in order to

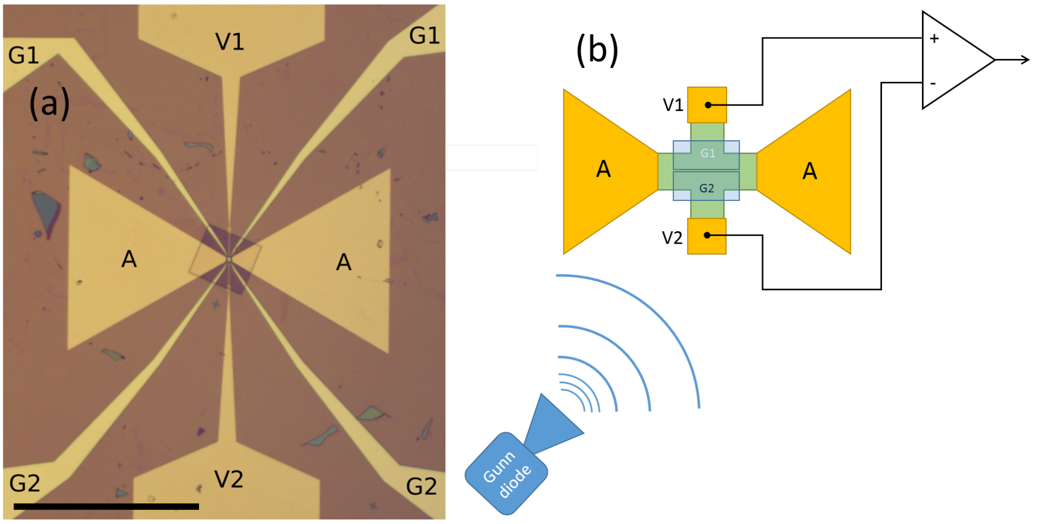

Figure 28: Optical image (a) and principle scheme (b) of radiation-detector prototype. The bow-tie antennas AA receive the radiation and convert it into AC current flowing across the $p-n$ junction. This AC current heats up the electron system and creates a temperature gradient. The TEP voltage occurs between the contacts V1 and V2. The scalebar in (a) is 500 μm. Adopted from Paper **III**.

minimize their impact on the antenna. For simplicity, we chose a broadband bow-tie type of antenna. This antenna receives the incoming radiation and creates AC current in the graphene channel. This current heats up the junction as in the DC device; the resulting TEP voltage is measured in open-circuit conditions. It is important to emphasize, that this bolometer does not need any current bias. We investigated the response of our detector to one radiation source - a Gunn diode with frequency of 94 GHz. The results are presented in Fig. 29. As with the DC thermoelectric device, we kept the difference between the voltages applied to the top gates constant $\delta V = \pm 2$ V, sweeping the average voltage $V_{av} = (V_{tg1} + V_{tg1})/2$. The TEP signal changed sign when δV changed sign. This is a clear indication of the thermoelectric origin of the signal. For the temperature range $4 - 100$ K we saw a weak temperature dependence of the TEP signal, similar to the DC device. However, at room temperature the signal from the bolometer was about 40 times lower. Since the radiation reached our detector from below (see Appendix: Methods and Recipes), the substrate partially screened the microwaves at room temperature, when even our low-doped Si remained conductive. Below 100 K, the charge-carriers in Si froze out allowing for the radiation penetration without significant losses. It would be definitely better

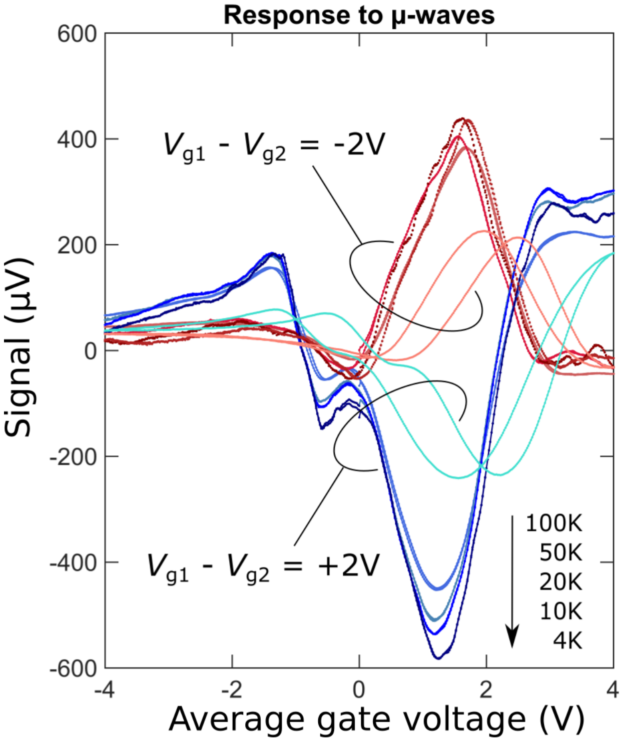

Figure 29: The TEP signal of radiation detector vs the average top-gate voltage for different temperatures. We see weak temperature dependence of the signal for $T = 10 - 100$ K. Adopted from Paper **III**.

to fabricate such detectors on, for example, quartz.

We estimated the power reaching the sample to be ~ 1 μW (see Appendix: Methods and Recipes). The maximum TEP signal ~ 400 μV gave in this case the responsivity value of $r = 400$ V/W for the temperature range $4 - 100$ K. Our measurement system had the noise level of 10 nV/Hz$^{0.5}$, which gave for our bolometer $NEP = 25$ pW/Hz$^{0.5}$ ($4 - 100$ K). The theoretical minimum noise calculated according to Johnson-Nyquist formula for $T = 4 - 300$ K was: $NEP_{JN} = \sqrt{4k_BTR}/r = 2.5 - 22$ pW/Hz$^{0.5}$. We compare these values with those of other detectors in the Discussion section.

After having carried out the simulations of the thermoelectric device (see Chapter 6), we decided to change the geometry and fabricate another radiation detector. An optical image of the bolometer with the new design is presented in Fig. 30. We replaced the bow-tie antenna with a log-periodic one and combined it with the gate electrodes. As a result, the antenna had only capacitive contact to the graphene device with $C = 17$ fF (this corresponds to the impedance $Z = -100i\ \Omega$ at 94 GHz). The $p - n$ junction direction coincided with the AC current direction, excluding the possibility of the hotspot appearance aside from the junction, which was the problem of the previous design.

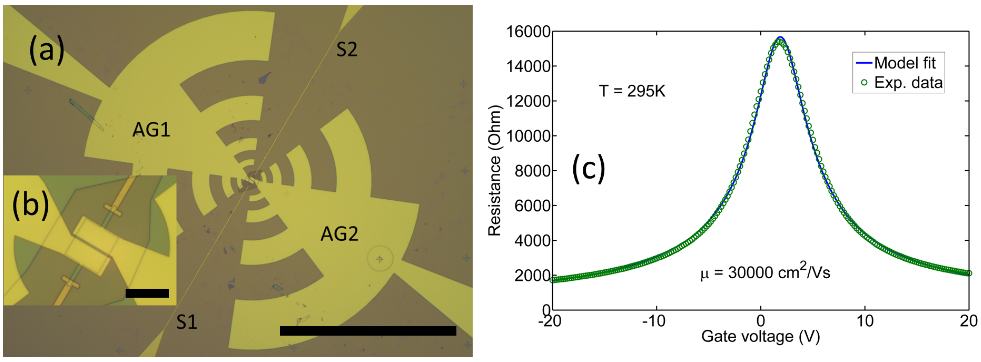

Figure 30: (a,b) Optical images of graphene bolometer with capacitive coupling to the antenna. AG1 and AG2 are the top gates combined with a log-periodic antenna; S1 and S2 are the read-out electrodes. The scale bars are 500 μm in (a) and 15 μm in (b). (c) Two-probe resistance between S1 and S2 as a function of back-gate voltage. The extracted mobility is $\mu = 30000$ cm^2/(V s), residual carrier concentration $n_0 = 1.3 \times 10^{11}$ cm^{-2}. Adopted from Paper **IV**.

For this bolometer, we measured the two-probe transfer curve and extracted $\mu = 30000$ cm^2/(V s) and $n_0 = 1.3 \times 10^{11}$ cm^{-2} from it (see Fig. 30(c)). This is actually the highest mobility achieved for graphene encapsulated in Parylene in this work.

Under irradiation, we measured the signal V_{TEP} as a function of the average top-gate voltage V_{av} with the fixed difference $\delta V = 0, \pm 1, \pm 2, \pm 4, \pm 8$ V for different temperatures. The results for $T = 50$ K are presented in Fig. 31(a). In order to compare the measurement results with theory, we derived analytical equations to simulate out data. For simplicity, we assumed that the TEP signal in our bolometer is the following:

$$V_{TEP} = [S(V_{tg1}) - S(V_{tg2})]\delta T, \tag{14}$$

where $S(V_{tg1})$ and $S(V_{tg2})$ are the Seebeck coefficients of the p and n parts of the junction and δT is the average electron overheating. For $S(V)$, we used Mott's formula:

$$S(V) = -\frac{2\pi^{\frac{3}{2}}}{3} \frac{k_B^2 T}{\hbar v_F \sqrt{e}} \frac{(C_g V)^{\frac{3}{2}}}{(e n_0)^2 + (C_g V)^2}, \tag{15}$$

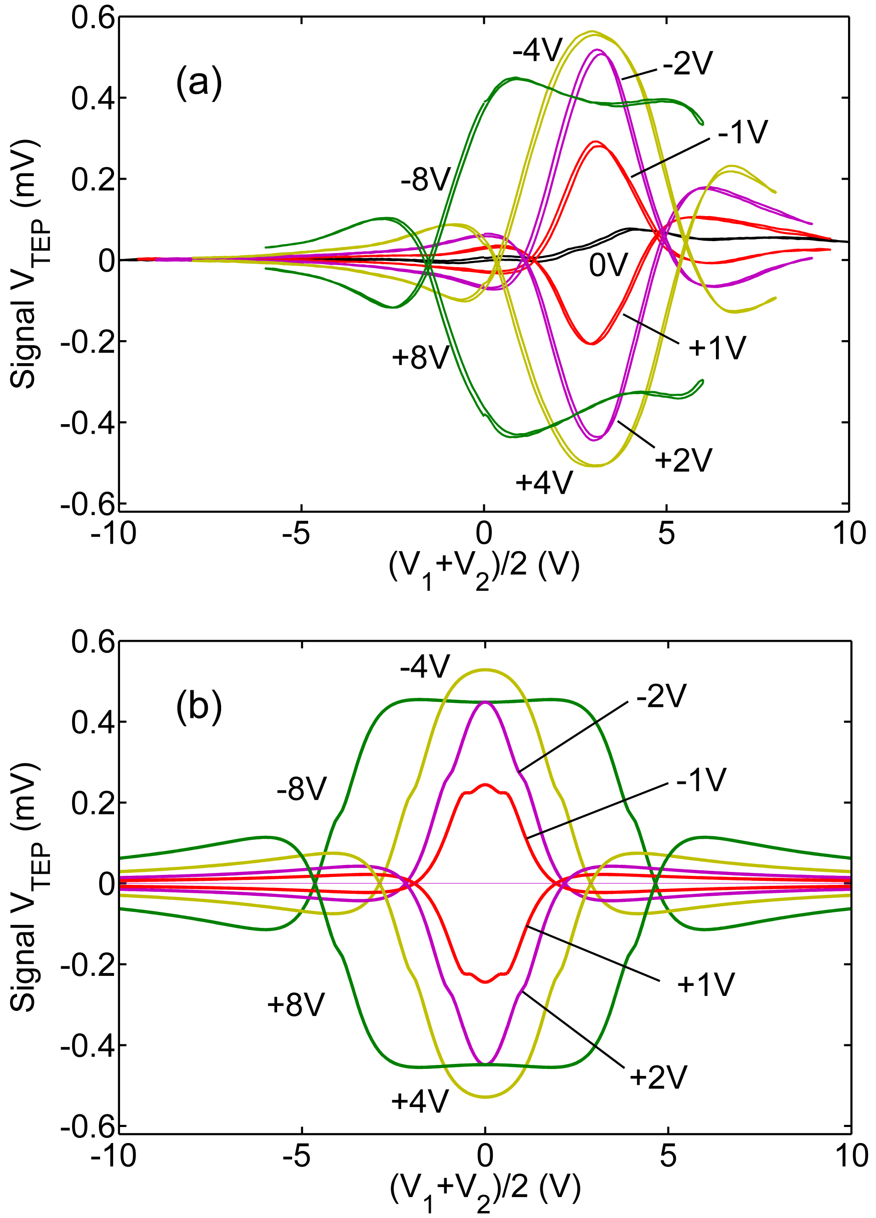

Figure 31: Experimental (a) and theoretical (b) plots of bolometer signal V_{TEP} as a function of the average top-gate voltage V_{av} for the fixed difference $\delta V = 0, \pm 1, \pm 2, \pm 4, \pm 8$ V at $T = 50$ K. The maximum signal occurs at $\delta V = \pm 4$ V both for theory and experiment. The values match at $\delta T = 7$ K. Other parameters for the calculations are: $n_0 = 1.0 \times 10^{11}$ cm^{-2} and $C_g = 1.5 \times 10^{-4}$ F/m^2. Adopted from Paper **IV**.

where $n_0 = 1.0 \times 10^{11}$ cm^{-2} is the residual carrier concentration, $C_g = 1.5 \times 10^{-4}$ F/m^2 is the gate capacitance per unit area, $v_F = 10^6$ m/s is the Fermi velocity in graphene, $\hbar$ is the Planck constant and k_B is the Boltzmann constant. In Fig. 31(b) we present the theoretical plot of the data from Fig. 31(a). We adjusted the amplitude of the theoretical curves to match the experimental value by choosing $\delta T = 7$ K. This is our estimation of electron overheating in this case. Qualitatively, we see good agreement between this simple model and the experiment. At $\delta V = 0$ V the theoretical signal is 0; the experimental curve shows very weak response. For $\delta V = -1, -2, -4$ V the signal represents a peak with growing amplitude, with the maximum signal at $\delta V = -4$ V. At $\delta V = -8$ V the peak decreases in intensity and splits into two. For positive δV the curves are mirrored against the $V_{TEP} = 0$ V axis. This comparison is one more argument for the bolometer signal to have a thermoelectric origin.

The temperature dependence of the bolometer signal at $\delta V = \pm 4$ V is presented in Fig. 32(a,b). As for the previous bolometer, we see a weak temperature dependence of the signal for $T = 4 - 100$ K. The weakness of the signal at room temperature was caused by the reason mentioned above: the Si substrate was slightly conductive and attenuated the power coming to the bolometer. At lower temperatures, the charge-carriers froze out and this attenuation vanished.

As mentioned above, the power reaching our device $P \sim 1$ μW. With the maximum signal of $V_{TEP} = 700$ μV, we get the value of responsivity $r \sim 700$ V/W. For this bolometer, we also performed the noise-level measurements at the point of the highest responsivity ($T = 50$ K, $\delta V = +4$ V). We reduced the power reaching the bolometer by a calibrated attenuator in the range of $0 - 50$ dB and measured the signal as a function of the attenuation (see Fig. 32(c)). The signal reached the noise plateau at 40 dB attenuation, which corresponds to $P \sim 100$ pW. With the equivalent noise bandwidth of 0.26 Hz it gave the estimation of the $NEP \sim 200$ pW/Hz$^{0.5}$.

5.4 Discussion and conclusions

The main comparable parameters of radiation detectors usually are: the operating frequency (wavelength) f (λ), the operating temperature T, the responsivity r and the noise equivalent power NEP. Comparison of our bolometers with some others is shown in Table 1.

For our bolometers, the operating frequency during the experiments was 94 GHz, but in principle, it should operate in the THz range as well. We plan to test it in future. However, in the IR range, where the wavelength becomes of the order of the device size, our bolometers would need chemical doping

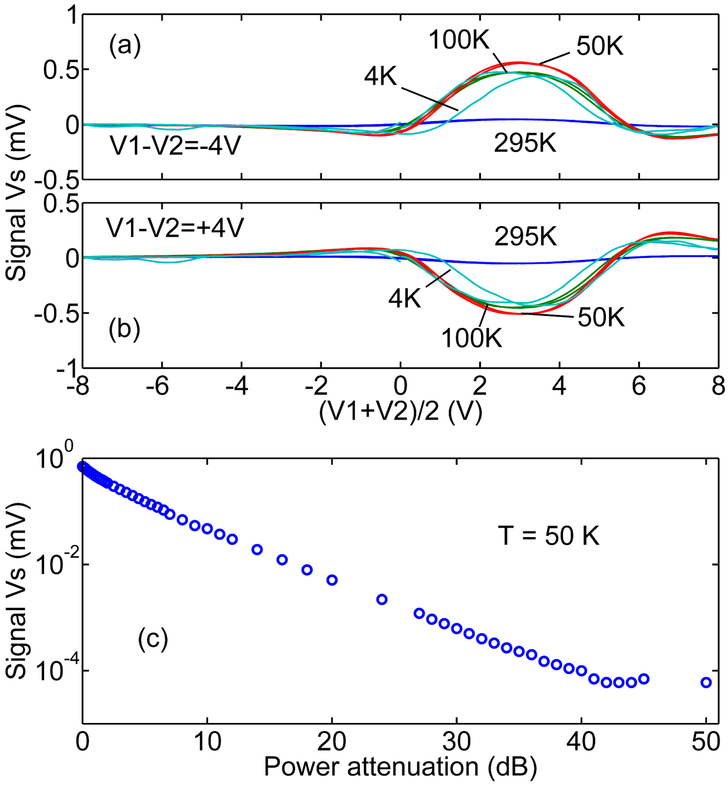

Figure 32: (a,b) The temperature dependence of the bolometer signal for $\delta V = \pm 4$ V. The signal is almost temperature independent for $T = 4 - 100$ K, but at $T = 293$ K it is strongly attenuated by the conducting Si substrate. (c) The signal as a function of the incoming power P. The noise plateau starts at 40 dB attenuation, which corresponds to $P \sim 100$ pW. Adopted from Paper **IV**.

instead of the top gates to avoid the screening of the most of the radiation.

The readout of our bolometers allows for operation in the wide temperature range $4 - 300$ K. Moreover, our bolometers showed weak temperature dependence of the signal for the temperatures $4 - 100$K and this range can be expanded up to 300 K, according to the results from our DC TE device.

Although the experimental setup was unoptimized, we measured the responsivity for our bolometer up to $r \sim 700$ V/W. This value is comparable with those of tunnel diodes (5000 V/W [89]) and MOSFETs (5000 V/W [90]) and is definitely better than that of graphene field-effect transistors (GFET) (74 V/W [83], 1.2 V/W [91]). However, Golay cells have substantially higher responsivity (10^5 V/W). One of the ways to improve the responsivity of our bolometer would be to achieve the matching of antenna and bolometer impedances. The theoretical impedance of the log-periodic antenna is $Z_A = 189\ \Omega$ [92], however, the impedance of the bolometer is $Z_{bol} \sim 10\ \mathrm{k}\Omega$. It means that the power received by the bolometer is about two orders of magnitude lower, than for the ideal case, when $Z_A = Z_{bol}$. Hence we can expect 100 times higher responsivity after impedance matching.

Detector type	Readout	f	T (K)	r (V/W)	NEP (pW/Hz$^{0.5}$)
TE HEB (this work)	Direct TE	94 GHz	4 – 300	700	200 (18*)
Golay cells [93]	dV/dT	IR, THz	300	10^5	140
SHEB [94]	dR/dT	THz	77 – 300	0.3	10
CEB [95]	dR/dT	345 GHz	0.28	2.4×10^9	2×10^{-5}
Tunnel diodes [89]	dI/dV	THz	300	5000	0.2
MOSFET [90]	dR/dP	THz	300	5000	10
MLG FET [83]	dR/dV_g	400 GHz	300	74	130
BLG FET [91]	dR/dP	THz	300	1.2	2000
MLG PD [96]	dI/dP	IR	300	0.61[c]	no data
BLG HEB [84]	dR/dP	IR	5	2×10^5	3.3×10^{-2}

Table 1: Comparison of high-frequency detectors. The abbreviation used in this table are: TE - thermoelectric, HEB - hot-electron bolometer, SHEB - semiconductor hot-electron bolometer, CEB - cold-electron bolometer, MOSFET - metal-oxide-semiconductor field-effect transistor, MLG - monolayer graphene, BLG - bilayer graphene, PD - photodetector.
* Theoretical minimum for $T = 300$ K, calculated from Johnson-Nyquist formula.

One more important parameter for a detector is the response time τ. For our devices it can be estimated as the ratio between the heat capacity of

---

[c] Recalculated from the original value 6.1×10^{-3} A/W.

electrons and the heat conductivity between electrons and phonons:

$$\tau = \frac{C_e n}{\frac{dP_{e-ph}}{dT_e}}, \tag{16}$$

where C_e, n and T_e are the electron heat capacity, electron concentration and electron temperature, respectively; P_{e-ph} is the coupling between electrons and phonons, which depends on the bath temperature (see Chapter 2). The Eq. 16 gives $\tau = 0.3$ fs for $T = 300$ K and $\tau = 1.2$ ps for $T = 4$ K. Such a fast response of our detectors comes from the low amount of electrons in the device ($\sim 1.5 \times 10^6$ electrons) and is faster than that for SHEB (50 ns) and substantially faster than that of Golay cells (10 ms).

The experimental value of $NEP = 200$ pW/Hz$^{0.5}$ for our bolometer was measured at $T = 50$ K. This is comparable to the room-temperature noise of Golay cells and GFET (140 pW/Hz$^{0.5}$). However our NEP is higher than that of SHEB (10 pW/Hz$^{0.5}$), tunnel diodes (0.2 pW/Hz$^{0.5}$) and MOSFETs (10 pW/Hz$^{0.5}$). We attribute the noise level in our experiments to the working cryostat compressor. The theoretical low limit of the noise level in our bolometer at $T = 300$ K can be calculated using Johnson-Nyquist formula: $NEP_{JN} = \sqrt{4k_BTR}/r = 18$ pW/Hz$^{0.5}$. There can also be 1/f-noise, which was observed in graphene devices [97], but due to no current bias, our bolometers may be free of this noise. Additional measurements are required to verify this.

The TE bolometers presented in this work showed competitive parameters even under unoptimized conditions. Both responsivity and NEP of our bolometers may be drastically improved after impedance matching with the antenna (decreasing the graphene resistance). Having weak temperature dependence of the output signal and fast response can make the TE bolometers beat the existing state-of-the-art detectors.

6 Computer simulations

Computer simulations are a very powerful tool to investigate complex systems. The simulations become especially useful when a corresponding experiment is difficult or impossible to carry out. In particular, temperature distributions are usually quite challenging to measure in real experiments. In this chapter, the computer simulations for the hybrid type CVD system and for the electron overheating in graphene are presented. We used the commercially available software COMSOL 4.1 and 5.2 for these simulations.

6.1 Heater simulations for CVD

The computer simulations for the hybrid type CVD system, discussed in Chapter 3, needed to visualize the temperature distributions the for single- and double heater setups and to support the benefits of the new design.

COMSOL includes physical models for Joule heating, heat transfer in solids, surface-to-surface- and surface-to-ambient radiation. We present an overview of the simulated system in Fig. 33. The cylindrical rods, as well as the rectangle washers, are made of molybdenum. The heaters are graphitic, the substrate for graphene growth is copper. For simplicity, we assume no gas around the heater and, thus, no heat transfer by convection. This is reasonable, since the pressure in the chamber did not exceed 10 mbar during the growth. We also did not take into account the thermal expansion of any materials, i.e. the geometry was independent of temperature. The graphite resistivity was taken to be linear in temperature, all the other physical values were set to be temperature independent. The bottom end of one of the rods was grounded, another was connected to DC voltage. Also, the temperature of the bottom ends of the rods was set to 293 K. The result of the calculation was the stationary temperature distribution, which resulted from a balance between the Joule power and the heat dissipated via radiation and thermal conductivity of the rods. During the real growth of graphene, the copper foil had the temperature close to the melting point of copper (1357 K). We compared the temperature distributions calculated for two setups (original and converted). In both cases we kept the temperature of the copper foil close to the melting point. This was done by adjusting the power of the heater which is defined by the voltage applied between the rods.

The meshing of the simulated objects was performed automatically by the software. The heaters and copper had a more precise mesh with the unit size ($\sim 100\ \mu m$) than the rods and washers ($\sim 500\ \mu m$). Since the copper was only $50\ \mu m$ thick, it had thickness of one mesh unit in the simulations.

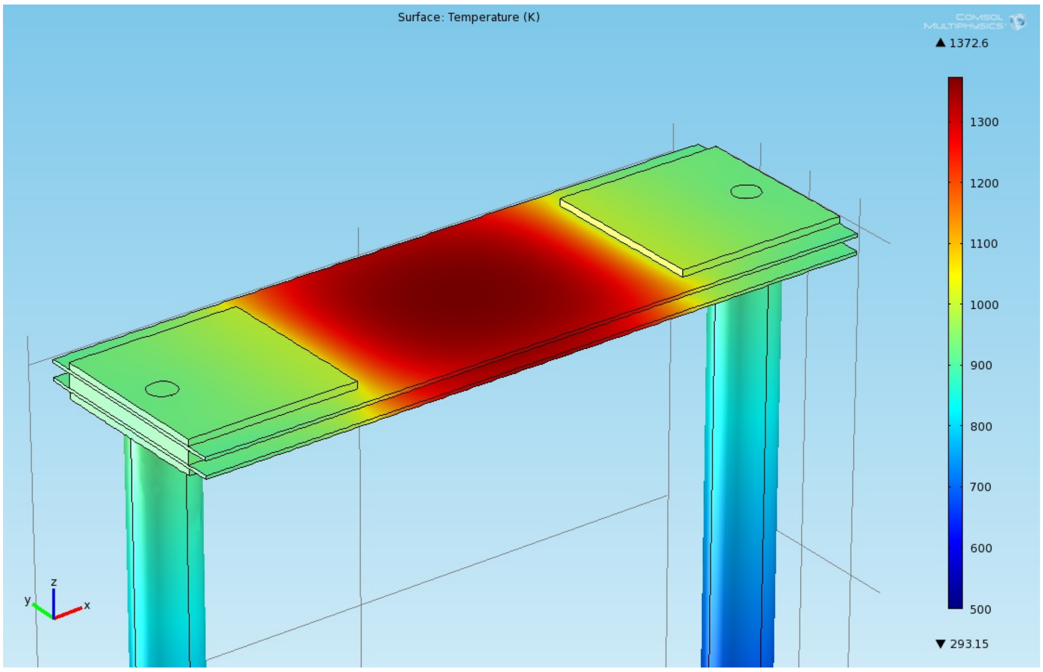

Figure 33: The plot of calculated temperature distribution for double heater setup. See also Fig. 9 in Chapter 3 for the parts description.

The stationary equations solved were the following:

$$\mathbf{E} = -\nabla V \tag{17}$$

$$\nabla \mathbf{J} = 0 \tag{18}$$

$$\mathbf{J} = \sigma \mathbf{E} \tag{19}$$

$$\nabla(\kappa \nabla T) + \mathbf{JE} - \varepsilon \Sigma (T^4 - T_{amb}^4) = 0,^{\mathrm{d}} \tag{20}$$

where $\mathbf{E}$, V, $\mathbf{J}$ and σ are the electric field, electric potential, current density, and conductivity, respectively; T, T_{amb}, κ, ε and Σ are the temperature, ambient temperature, thermal conductivity, surface emissivity, and Stefan Boltzmann constant, respectively.

In Fig. 34 we present the temperature distributions across the copper foil and the heater for both setups. We see that for our new setup both the heater and the foil have a more homogeneous temperature and the temperature of the foil is much closer to the temperature of the heater than in the original single-heater setup. The difference between the maximum and minimum

---

[d] This is a simplified equation. In fact, the T_{amb} depended on the surfaces in the vicinity of the current point.

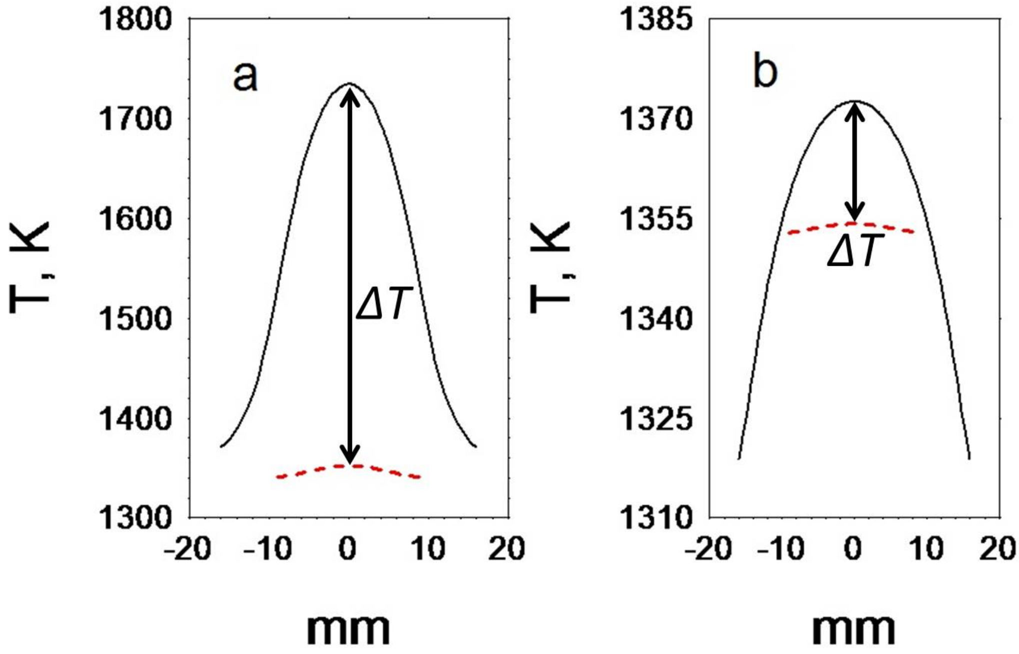

Figure 34: Comparison of the temperature distributions along the middle line of the copper foil for the single- (a) and double heater (b) setups. The solid lines correspond to the heater temperature, the dashed lines correspond to the foil temperature. In the double-heater setup, the heater is much less overheated against the foil as in the single-heater setup. Adopted from Paper **I**.

temperature of the foil is 10 K for the original setup and only 1.2 K for the new one. As discussed in Chapter 3, the temperature affects the nucleation of graphene. Hence, a more uniform temperature distribution results in a more homogeneous CVD graphene film and a better reproducibility of graphene devices.

The simulations showed how nonuniform can be the temperature distribution of a heated copper foil despite its high thermal conductivity. The results obtained convinced us of the importance of the way the foil is heated in a CVD system. It was also helpful to visualize the temperature distributions, since this data could not be obtained in experiment.

6.2 Simulations of hot-electron effects

In order to visualize electron overheating and verify the position of the hot spot in our thermoelectric device (see Chapter 5), we performed computer simulations of the hot-electron effects. We assumed two different subsystems in graphene - the phonons and electrons - having a weak coupling between them [43, 44]. The physics included the Joule heating, thermoelectric effects (including Peltier effect), and heat transfer. The Joule power was generated by electrons and dissipated further to the electrodes and out-of-plane to the substrate. The solution represented a stationary distribution of electron- and phonon temperatures. The main parameters were the current I injected into the graphene device and the bath temperature T_0.

The equations used in our model are the following:

$$\mathbf{E} = -\nabla V \tag{21}$$

$$\nabla \mathbf{J} = 0 \tag{22}$$

$$\mathbf{J} = \sigma(\mathbf{E} - S\nabla T_e) \tag{23}$$

$$\nabla(\kappa_e \nabla T_e) + \mathbf{JE} - T_e \mathbf{J} \nabla S - P_{e-ph} = 0 \tag{24}$$

$$\nabla(\kappa_{ph} \nabla T_{ph}) + P_{e-ph} - P_{sub} = 0, \tag{25}$$

where $\mathbf{E}$, V, $\mathbf{J}$ are the electric field, electric potential, and current density, respectively; σ, S, κ_e (κ_{ph}), T_e (T_{ph}) are the graphene electrical conductivity, Seebeck coefficient, electron (phonon) thermal conductivity, electron (phonon) temperature, respectively; P_{e-ph} is the coupling between electrons and phonons; P_{sub} is the power dissipated into the substrate.

The resistivity of graphene was calculated according to:

$$\sigma = \mu\sqrt{(en_0)^2 + [C_{tg}V_{tg} - (C_{tg} + C_{bg})V]^2} \tag{26}$$

where μ, n_0, C_{tg}, C_{bg}, V_{tg}, V, and e are the mobility, residual carrier concentration, top-gate- and bottom-gate specific capacitances, voltage applied to the top gate, potential in the current point, and electron charge, respectively. This formula results from Eq. 2, taking into account the self-gating effect. We assumed the graphene conductivity to be temperature independent, since it does not have a strong temperature dependence in reality for supported graphene. The values of $\mu = 5000$ cm^2/(V s) and $n_0 = 3 \times 10^{11}$ cm^{-2} were taken as average results from the experiments with the same kind of samples (see Chapter 4). The value of $C_{tg} = 1.3 \times 10^{-4}$ F/m^2 corresponds to 180 nm Parylene N and $C_{bg} = 1.13 \times 10^{-4}$ F/m^2 corresponds to 90 nm SiO$_2$ and 150 nm Parylene N.

The Seebeck coefficient was calculated from Mott's formula, including the self-gating effect:

$$S = -\frac{2\pi^{1.5}}{3}\frac{k_B^2 T_e}{\hbar v_F\sqrt{e}}\frac{(C_{tg}V_{tg} - (C_{tg} + C_{bg})V)^{1.5}}{(en_0)^2 + (C_{tg}V_{tg} - (C_{tg} + C_{bg})V)^2} \tag{27}$$

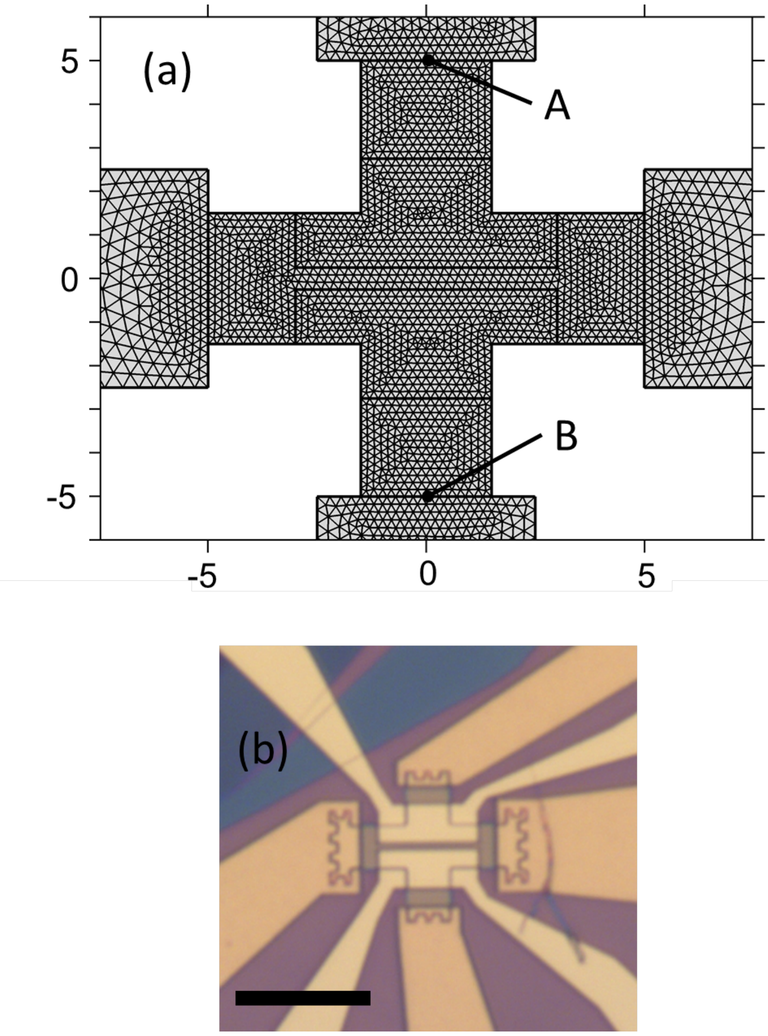

Figure 35: The meshing of the simulated device (a) and a photo of a real device (b). The axes in (a) are in μm. The scale bar in (b) is 10 μm. The size of the simulated device is the same as the real one. The mesh has the unit size $\sim$ 0.25 μm for graphene and becomes $\sim$ 1 μm for the gold electrodes. The mesh presented here is three times larger than in the real simulation, to provide a better look. The zigzag edges of the contacts were not included in the simulation to simplify the mesh. The signal V_{TEP} was calculated and the potential difference between the points A and B.

where k_B, $\hbar$ and v_F are the Boltzmann constant, reduced Planck constant and Fermi velocity in graphene, respectively.

The thermal conductivity of electrons was measured experimentally [40]: $\kappa_e(T_e) = \gamma(\frac{T_e}{300K})^{1.6}$, where $\gamma = 6.8$ W/(K m). The phonon thermal conductivity was set as temperature independent, $\kappa_{ph} = 600$ W/(K m) [39]. The coupling between electrons and phonons was taken as $P_{e-ph} = \alpha(T_e^3 - T_{ph}^3)$, $\alpha = 0.5$ W/(K^{3}m^2) for high temperatures ($T_{ph} > T_{BG}$) [98] and $P_{e-ph} = \beta(T_e^4 - T_{ph}^4)$, $\beta = 2 \times 10^{-3}$ W/(K^{4}m^2) for low temperatures ($T_{ph} < T_{BG}$) [99]. T_{BG} is the Bloch-Grüneisen temperature, which is defined as $k_B T_{BG} = 2k_F v_{ph}$, where k_F is the Fermi wave vector and v_{ph} is the phonon velocity in graphene.

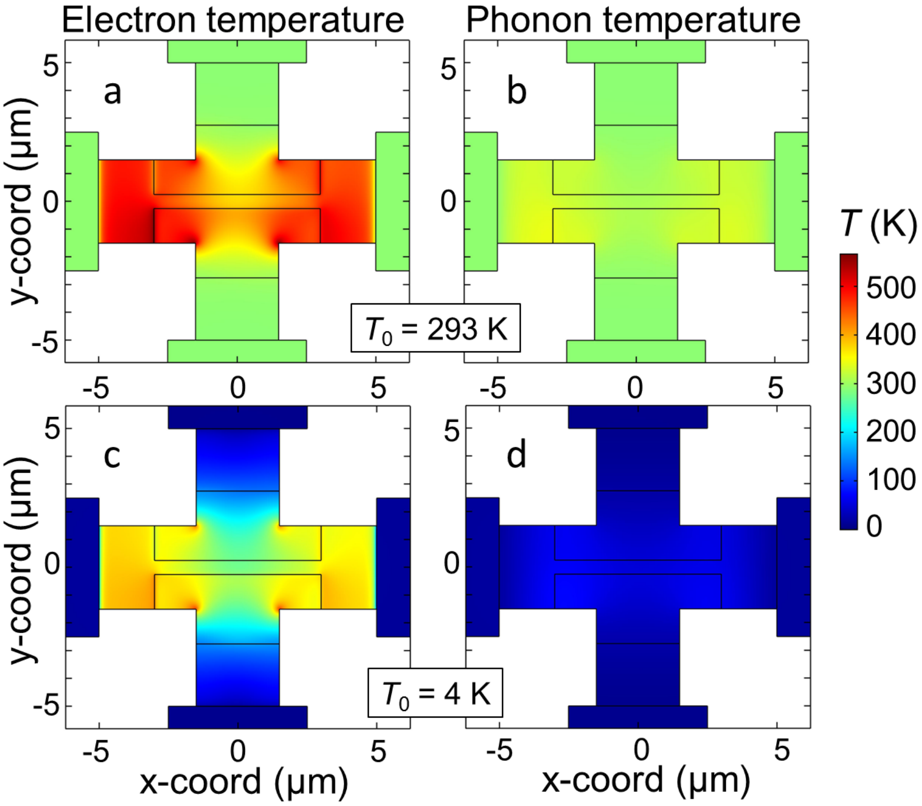

Figure 36: The plots of calculated temperature distributions in thermoelectric graphene device biased to $I = 300$ μA for two bath temperatures $T_0 = 293$ K and $T_0 = 4$ K. We see significant difference in electron and phonon temperatures, especially for low bath temperature. Adopted from Paper **III**.

The electrodes were assumed to be made of golden thin film 200 nm thick; all the required physical values for gold were taken from the COMSOL materials library. The power dissipation via the substrate was modelled as an out-of-plane heat flow with the power $P_{sub} = \kappa_{Par}(T_{ph} - T_0)/d$ where κ_{Par} is the thermal conductivity of Parylene and d is the thickness of Parylene layer. The Parylene thermal conductivity at room temperature is known [74], however, there is no information in literature about its temperature dependence. We assumed it to be similar to that of PMMA [100] and described it by the linear equation $\kappa_{Par} = 1.8 \times 10^{-2} + 3.6 \times 10^{-4} T_{ph}$ W/(K m).

The boundary conditions for our simulations were the following. The device was considered to be in vacuum, the edges of graphene were thermally- and electrically isolated except for the contact areas to the electrodes. There was no thermal- or electrical contact resistance between graphene and gold. One of the horizontal electrodes was grounded, another was biased to DC current I. Both graphene and gold had the out-of-plane thermal contact with the substrate.

We performed calculations for several bath temperatures within the range $T_0 = 4-293$ K and for the incoming powers $P = 1$ μW $-$ 1 mW. The electron- and phonon temperature distributions for $P = 1$ mW are presented in Fig. 36 for $T_0 = 4$ and 293 K. We see a significant overheating of the electron system: for $T_0 = 293$ K, the difference between the maximum electron and phonon temperatures is 200 K. For $T_0 = 4$ K, it is even higher - 350 K. This overheating agrees qualitatively well with the experimental data from the shot-noise measurements [98]. From these simulations we also see that the maximum electron temperature occurs away from the middle of the graphene device, making the temperature gradient contributing to the thermoelectric (TEP) voltage lower.

The TEP signal was directly obtained from the calculations as the difference between the electric potentials of the two vertical electrodes (points A and B in Fig. 35). We present the TEP voltage vs bath temperature for various input powers in Fig. 37(a). From this plot we see that the signal is almost temperature independent for high power and even increases with decreasing temperature for low power. This partially agrees with our experiments: we saw almost no temperature dependence of the TEP signal for high power. In Fig. 37(b) we present a plot of the TEP signal as a function of the bias current and the back-gate voltage. It is similar to the experimental plot in Fig. 27 (Chapter 5). Here we see good qualitative agreement between the experiment and the simulations, which indicates the thermoelectric origin of the signal. Also, the self-gating effect, included in the model, accounts for the relative shift of the signal maxima along the V_{bg}-axis.

To conclude, we performed computer simulations of thermoelectric graphene device, which showed good qualitative agreement with the experimental data at high power. At low power our simulations deviated from the high-frequency experimental data, since we did not consider the capacitive coupling to the top gates in our DC simulations. Our simulations also revealed

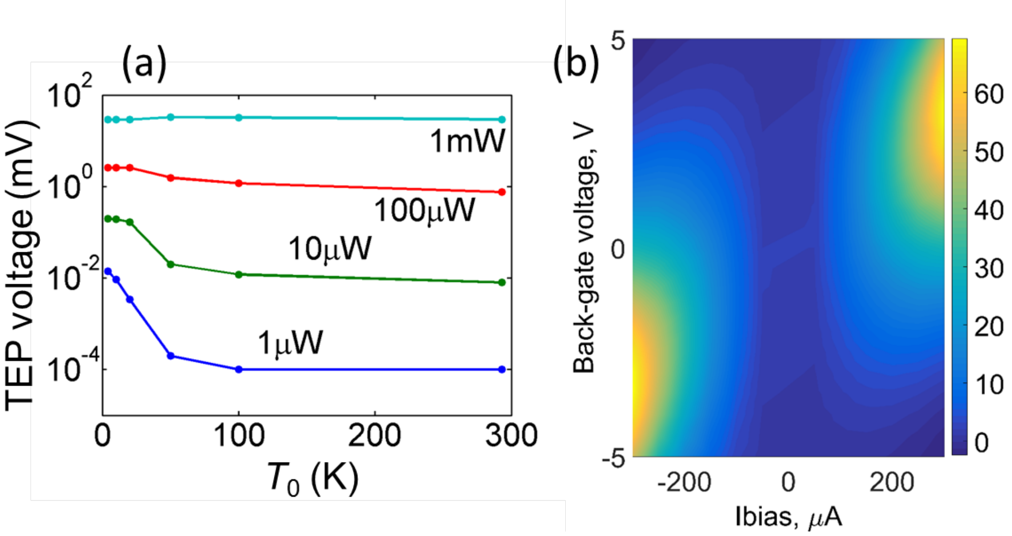

Figure 37: (a) Calculated TEP voltage vs bath temperature T_0 and power P. Adopted from Paper **III**. (b) A false-color plot of the calculated TEP voltage vs the bias current I and the back-gate voltage V_{bg} at $T = 300$ K. This plot has good qualitative agreement with Fig. 27 in Chapter 5. The color scale is in mV. Adopted from Supplementary for Paper **III**.

the temperature distributions in our thermoelectric devices and indicated that the position of the hotspot was not ideal. This helped us to improve the hotspot position in the redesigned bolometer with capacitively coupled antennas.

7 Summary and conclusions

We developed a technology for graphene encapsulation and device fabrication and used it to build prototypes of radiation detectors based on thermoelectric effects.

We used Parylene N to encapsulate graphene. We demonstrated the possibility to fabricate the edge-contacts to graphene with contact resistivity down to 14 $\Omega \cdot \mu$m. We fabricated Hallbar devices to investigate the quality of graphene. The samples had room temperature charge-carrier mobility up to 30000 cm^2/Vs, residual carrier concentration down to 10^{11} cm^{-2} and the Dirac point close to zero. These parameters allow for a wide range of applications. We also demonstrated the scalability of this technology by fabricating large-scale devices from CVD graphene.

The DC thermoelectric device showed a clear thermoelectric response with the responsivity up to 90 V/W, which was almost independent on temperature. We associate this high responsivity with the hot-electron effects and the high value of Seebeck coefficient in graphene. We also performed computer simulations of the thermoelectric- and hot-electron effects in the devices and saw good qualitative agreement with the experiment.

To test the applicability of such a device, we fabricated a prototype of radiation detector. We illuminated it with 94 GHz radiation and measured responsivity up to 400 V/W under unoptimized conditions. We saw a weak temperature dependence of the signal in the temperature range $4 - 100$ K. The signal at 293 K was limited by the low-doped Si substrate, which had some conductivity and attenuated the incoming power. The estimation of the noise level of this detector gave a value of $NEP = 25$ $\text{pW}/\text{Hz}^{0.5}$.

As a development of the design, we fabricated a detector with purely capacitive coupling to antennas. This detector featured a very simple four-contact geometry, where the external gates were combined with the antennas. This detector showed responsivity up to 700 V/W for 94 GHz radiation. The responsivity had weak temperature dependence for the temperature range $4-100$ K, and was limited at 293 K due to the same reason, mentioned above. The theoretical estimations of the response time gave the value $\tau < 1.2$ ps. The noise measurements at 50 K gave us the minimum value of $NEP = 200$ $\text{pW}/\text{Hz}^{0.5}$. The estimation based on the Johnson - Nyquist formula gave a ten times lower $NEP = 18$ $\text{pW}/\text{Hz}^{0.5}$.

The presented detectors showed competitive parameters and after optimization could be possibly used in applications, which require fast response and wide operating temperature range.

Appendix: Methods and Recipes

Exfoliation of graphene on SiO_2/Si

There is no universal recipe of graphene exfoliation. In each lab it is slightly different due to different available materials. The process itself looks quite simple. However, close attention should be paid to small details of the process, since the final result depends on many parameters. Here we present the recipe, which was optimized in the cleanroom in Chalmers University of Technology and gives the largest flakes with high yield. The substrates used are SiO_2/Si chips with $285-300$ nm oxide thickness.

- Prepare the target substrate: sonicate in acetone for 3 mins, rinse in isopropanol (IPA) and blow dry with nitrogen.
- Cut a rectangle around 15×150 mm out of the sticky tape, remove the covering film, press the sticky side to a piece of natural graphite and release.
- Cleave the graphite pieces left on the sticky tape 5-7 times, spreading them along the tape.
- Cut rectangles around 12×25 mm out of another fresh piece of sticky tape, their size and number of them should correspond to that of the target substrates.
- Stick these small rectangles to the cleaved graphite with sticky side.
- Finally clean the substrates in O_2-plasma for at least 3 mins at 250 W, 500 mTorr.
- Immediately after opening the plasma machine chamber detach the small rectangles, which now should have some cleaved graphite on them, and press them to corresponding substrates.
- Heat the samples on a hot plate at 110° C for 3 mins.
- Remove the samples from the hotplate, let them cool down for 1 min and slowly detach the sticky tape.
- Observe the result under an optical microscope.

Exfoliation of graphene on Parylene/SiO_2/Si

This recipe consists of two parts: substrate preparation and exfoliation itself. The second part resembles the previous recipe with minor changes. Preparation of the Parylene/SiO_2/Si substrates:

- Start from a SiO_2/Si substrate with 90 nm oxide thickness, sonicate in acetone for 3 mins, rinse in IPA and blow dry with nitrogen.
- Finalize cleaning in O_2-plasma for at least 3 mins at 250 W, 500 mTorr.
- Immediately load the substrates into the Parylene coating machine and pump it down.
- Deposit 150 nm of Parylene. For the SCS PDS 2010 Labcoter the weight of the precursor should be 1.60 g with the base/process pressures 10/12 mbar respectively.

Since the Parylene is vulnerable to O_2-plasma, it is recommended not to unload the substrates from the Parylene deposition machine until the following exfoliation step:

- Cut a rectangle around 15×150 mm out of the sticky tape, remove the covering film, press the sticky side to a piece of natural graphite and release.
- Cleave the graphite pieces left on the sticky tape 5-7 times, spreading them along the tape.
- Cut rectangles around 12×25 mm out of another fresh piece of sticky tape, their size and number of them should correspond to that of the target substrates.
- Stick these small rectangles to the cleaved graphite with sticky side.
- Detach the small rectangles from the main tape and press them to the substrates individually.
- Heat the samples on a hot plate at 110° C for 3 mins.
- Remove the samples from the hotplate, let them cool down for 1 min and slowly detach the sticky tape.
- Observe the result under an optical microscope.

For this substrate (150 nm Parylene / 90 nm SiO_2 / Si) the contrast of graphene should be similar to that on the conventional substrate (290 nm SiO_2/Si).

Patterning Parylene/graphene/Parylene structures using electron beam lithography

This recipe was used on EBL machine JEOL JBX9300FS with quite expensive resist ZEP 520A. The latter can possibly be replaced by ARP series resists, but the parameters of the recipe will then change. The patterning of a Parylene/graphene/Parylene structure consists of the following steps:

- Spin coat the sample with ZEP 520A at 4000 rpm, bake at 160° C for 5 mins.
- Expose in EBL system with the dose 300 μC/μm^2.
- Develop in O-xylene for 1:00 min (this is a very important parameter), rinse in IPA, blow dry with nitrogen.
- Etch in O_2-plasma for 90 s at 40 W and 250 mTorr.
- Remove the ZEP resist in Remover 1165 during several hours (overnight).

Fabricating contacts to Parylene/graphene/Parylene devices

- Spin coat the sample with Copolymer MMA(8.5) EL10 at 4000 rpm, bake at 160° C for 5 mins.
- Spin coat the sample with PMMA 950 EL2 at 4000 rpm, bake at 160° C for 5 mins.
- Expose in EBL system with the dose 300 μC/μ^2.
- Develop in MIBK:IPA 1:1 for 1:30 min, rinse in IPA, blow dry with nitrogen.
- Deposit Cr (1 nm) / Pd (15 nm) / Au (200 nm) in evaporator.
- Liftoff in acetone for 1 hour, no sonication.

Patterning graphene using photolithography

This recipe was used with very common photoresists S1813 and S1805. The choise between these two resists depended on the required etching time: the longer the planned etching time, the thicker resist is needed. The exposure was done on Canon PPC-210 projection mask aligner.

- Spin coat the sample with S1813 (S1805) at 3000 rpm, bake at 100° C for 1 min.
- Expose 30 (20) s.
- Develop in MF319 for 30 (20) s, rinse in DI water, blow dry with nitrogen.
- Etch in O_2-plasma for the required time depending on the thickness of the etched material. Monolayer graphene - 10 s at 40 W and 250 mTorr, for x nm Parylene - $1.5x$ s at 40 W and 250 mTorr.
- Flush expose the remaining resist without a mask with double the time used for general exposure. This is done to ease the subsequent resist removal.
- Remove the resist during 1 h in acetone.

Liftoff process using photolithography

This recipe was used with a very common photoresist S1813. The exposure was done on Canon PPC-210 projection mask aligner.

- Spin coat the sample with S1813 at 3000 rpm, bake at 100° C for 1 min.
- Expose 30 s.
- Put in toluene for 2 mins to subsequently create an undercut required for liftoff process.
- Develop in MF319 for 30 (20) s, rinse in DI water, blow dry with nitrogen.
- Flush expose the remaining resist without a mask with double the time used for general exposure. This is done to ease the subsequent liftoff.
- Liftoff during 1 h in acetone.

Wet transfer of CVD graphene (etching)

This recipe was used to transfer CVD graphene from copper foil to SiO_2/Si substrate.

- Spin coat the graphene with PMMA 950 A4 at 1000 rpm, bake at 120° C for 5 mins.
- Repeat the previous step to achieve thicker PMMA layer.
- Cut a frame out of thermorelease tape, stick it to the back side of the foil.
- Burn the back side graphene in O_2-plasma.
- Put the foil in a glass with 0.5M water solution of $(NH_4)_2SO_4$. Etch during 1-2 h depending on the thickness of the foil, constantly stirring the solution.
- After the hole in the frame becomes transparent, take the sample out an wash in warm (80° C) DI water several times.
- Clean the SiO_2/Si substrate the same way as describe above for exfoliation recipe.
- Put a droplet of DI water on the substrate, take the PMMA/graphene film out of water and bring it in contact with the substrate.
- Leave for drying for several hours (overnight).
- Cut away the frame and bake the sample at 120° C for at least 30 mins to achieve good adhesion.
- Dissolve PMMA in warm (50° C) acetone.
- (Optional) Anneal the sample in Ar/H_2 atmosphere at $400 - 1000^\circ$ for several hours to remove the remainings of PMMA.

Wet transfer of CVD graphene (bubbling)

- Spin coat the graphene with PMMA 950 A4 at 1000 rpm, bake at 120° C for 5 mins.
- Repeat the previous step to achieve thicker PMMA layer.
- Cut a frame out of thermorelease tape, stick it to the back side of the foil.
- Burn the back side graphene in O_2-plasma.

- Connect the foil and another piece of inert metal (platinum) to (-) and (+) electrodes of DC power supply respectively. Immerse them both in a 0.01M water solution of $NaSO_4$.
- Wait until the H_2 bubbles separate the PMMA film with graphene from the foil. The bubbling intensity can be tuned by the voltage output.
- After the film is completely separated from the foil, take the sample out an wash in warm (80° C) DI water several times.
- Clean the SiO_2/Si substrate the same way as describe above for exfoliation recipe.
- Put a droplet of DI water on the substrate, take the PMMA/graphene film out of water and bring it in contact with the substrate.
- Leave for drying for several hours (overnight).
- Cut away the frame and bake the sample at 120° C for at least 30 mins to achieve good adhesion.
- Dissolve PMMA in warm (50° C) acetone.
- (Optional) Anneal the sample in Ar/H_2 atmosphere at $400 - 1000°$ for several hours to remove the remainings of PMMA.

Experimental setup for bolometric measurements

The setup used for our microwave measurements in presented in Fig. 38. We used the pulse-tube cryostat Janis PT450 which had optical windows transparent for microwaves and allowed for measurements at temperatures $4 - 300$ K. The sample was mounted with its backside to a silicon lens. As a radiation source we used a Gunn oscillator (QuinStar Technology) with output frequency 94 GHz and power 30 mW. It was connected to a horn antenna through an adjustable attenuator 0-60 dB. For the signal modulation we used a mechanical chopper $7 - 900$ Hz and a lock-in amplifier DSP SR850 to synchronously detect the signal. Another attenuator was placed between the chopper and the cryostat window. Its was made from two Si wafers put together at 45° providing almost polarization independent attenuation of 20 dB. The signal from the lock-in amplifier went through instrumentation amplifiers APM01 with 1000x gain. This setup did not have any additional filters, so the minimum noise level was $10 - 20$ nV/Hz$^{0.5}$, but it increased when the compressor was turned on.

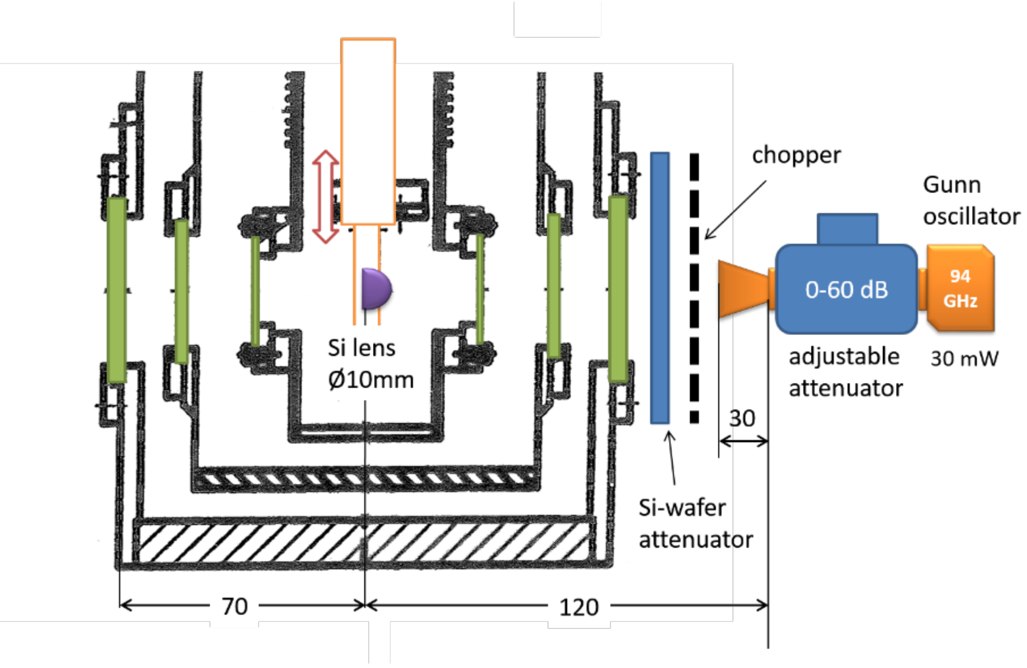

Figure 38: Experimental setup for our bolometers measurements. Adopted from Supplementary for Paper **III**.

The Si lens was mounted on a vertical rod, which could be rotated and moved up and down. The Gunn diode was also movable. This helped to find the best sample- and source positions for the maximum received power.

Acknowledgements

First of all, I want to thank my main supervisor and examiner August Yurgens for those years of guidance and help. I was very happy to be invited for short visits to Chalmers in 2012-2013 and then to be admitted as a PhD student.

Many thanks to Jie Sun, my co-supervisor, for interesting discussions and hand-on training in the lab.

Niclas, thank you for the time spent together in the lab, I really enjoyed working with you!

I am also very thankful to Ken Teo for hospitality during my visits to AIXTRON. It was very useful for me to look at graphene from the industrial point of view.

Thanks to my officemate Mengyue, for creative working atmosphere and discussions from science to politics!

Alexey Kalaboukhov, thank you very much for teaching me lots of useful thing. Your ability to find some time when you do not have it is amazing!

Samuel, thank you for interesting discussions and collaboration experience!

I am also grateful to Mikhail Tarasov for fruitful discussions about bolometers and antennas.

I want to thank Martin Hollertz, Mattias Fredrikson, Mats Hagberg, Henrik Fredriksen, Göran Alestig, Johan Andersson, Bengt Nilsson and all other cleanroom staff for training, advices and equipment support.

I am grateful to Lars and Stefan for the help in the workshop and to Susannah, Maria and Debora for the administrative support.

Tusen tack to Niclas and Eric for speaking Swedish with me, even when I could say only a few words. That helped me believe that one day I can speak this language fluently.

Thanks to all past and present QDP members for creating a wonderful working environment!

Many, many thanks to my family: my parents Marina and Mikhail, who convinced me to study Physics and English from the very young age; my wife Zhenya, for the support and understanding (even when I was working on weekends); my brother Viktor, and, of course, my little daughter Alexandra!

List of abbreviations

1D, 2D, 3D	one-, two-, three-dimensional
AC	Alternating current
AFM	Atomic force microscope
BLG	Bilayer graphene
CEB	Cold-electron bolometer
CVD	Chemical vapour deposition
DC	Direct current
DI water	Deionized water
EBL	Electron-beam lithography
FET	Field-effect transistor
hBN	Hexagonal boron nitride
HEB	Hot-electron bolometer
IPA	Isopropanol
MLG	Monolayer graphene
MOSFET	Metal-oxide-semiconductor field-effect transistor
ND	Nucleation density
NEP	Noise-equivalent power
PD	Photodetector
PDMS	Polydimethylsiloxane
PMMA	Polymethylmethacrylate
PPC	Polypropylene Carbonate
QHE	Quantum Hall effect
SHEB	Semiconductor hot-electron bolometer
SEM	Scanning electron microscope
TE	Thermoelectric
TEP	Thermoelectric power

List of symbols

B	magnetic field
C_e	electron heat capacitance
C_g	specific gate capacitance
C_{ph}	phonon heat capacitance
e	elementary charge
$\mathbf{E}$	electric field vector
g_s	degeneracy factor
$\hbar$	reduced Planck constant
I	electric current
$\mathbf{J}$	current density vector
$\mathbf{k}$	wave vector
k_B	Boltzmann constant
k_F	Fermi wave vector
k_x,k_y	wave vector components
l_e	electron mean free path
n	charge-carrier concentration
n_0	residual carrier concentration
$N_\square$	geometrical number of squares
P_{e-ph}	electron-phonon coupling
P_{sub}	power, dissipated into the substrate
$\mathbf{q}$	heat flux
R	universal gas constant
R_c	contact resistance
R_H	Hall constant
S	Seebeck coefficient
T	temperature
T_{BG}	Bloch-Grüneisen temperature
T_e	electron temperature
T_{ph}	phonon temperature

V_D	Dirac voltage
v_F	Fermi velocity
V_g	gate voltage
κ_e	electron heat conductivity
κ_{Par}	Parylene heat conductivity
κ_{ph}	phonon heat conductivity
μ	charge-carrier mobility
ν	filling factor
Π	Peltier coefficient
Σ	Stefan Boltzmann constant
σ	conductivity

References

[1] K. S. Novoselov, A. K. Geim, S. V. Morozov, D. Jiang, Y. Zhang, S. V. Dubonos, I. V. Grigorieva, and A. A. Firsov. Electric field effect in atomically thin carbon films. *Science*, 306(5696):666–669, 2004.

[2] K. S. Novoselov, A. K. Geim, S. V. Morozov, D. Jiang, M. I. Katsnelson, I. V. Grigorieva, S. V. Dubonos, and A. A. Firsov. Two-dimensional gas of massless dirac fermions in graphene. *Nature*, 438(7065):197–200, 2005.

[3] K. S. Novoselov, Z. Jiang, Y. Zhang, S. V. Morozov, H. L Stormer, U. Zeitler, J. C. Maan, G. S. Boebinger, P. Kim, and A. K. Geim. Room-temperature quantum hall effect in graphene. *Science*, 315(5817):1379–1379, 2007.

[4] P. R. Wallace. The band theory of graphite. *Physical Review*, 71(9):622, 1947.

[5] G. Ruess and F. Vogt. Höchstlamellarer kohlenstoff aus graphitoxyhydroxyd. *Monatshefte für Chemie/Chemical Monthly*, 78(3):222–242, 1948.

[6] H.-P. Boehm, A. Clauss, G. O. Fischer, and U. Hofmann. Das adsorptionsverhalten sehr dünner kohlenstoff-folien. *Zeitschrift für anorganische und allgemeine Chemie*, 316(3-4):119–127, 1962.

[7] P. Blake, E. W. Hill, A. H. Castro Neto, K. S. Novoselov, D. Jiang, R. Yang, T. J. Booth, and A. K. Geim. Making graphene visible. *Applied Physics Letters*, 91(6), 2007.

[8] Y. Zhang, Y.-W. Tan, H. L. Stormer, and P. Kim. Experimental observation of the quantum hall effect and berry's phase in graphene. *Nature*, 438(7065):201–204, 2005.

[9] C. Lee, J. W. Wei, X.and Kysar, and J. Hone. Measurement of the elastic properties and intrinsic strength of monolayer graphene. *Science*, 321(5887):385–388, 2008.

[10] K. I. Bolotin, K. J. Sikes, Z. Jiang, M. Klima, G. Fudenberg, J. Hone, P. Kim, and H. L. Stormer. Ultrahigh electron mobility in suspended graphene. *Solid State Communications*, 146(9):351–355, 2008.

[11] X. Li, W. Cai, J. An, S. Kim, J. Nah, D. Yang, R. Piner, A. Velamakanni, I. Jung, E. Tutuc, S. K. Banerjee, L. Colombo, and R. S. Ruoff. Large-area synthesis of high-quality and uniform graphene films on copper foils. *Science*, 324(5932):1312–1314, 2009.

[12] S. Bae, H. Kim, Y. Lee, X. Xu, J.-S. Park, Y. Zheng, J. Balakrishnan, T. Lei, H. Ri Kim, Y. I. Song, Y. Kim, K. S. Kim, B. Özyilmaz, J.-H. Ahn, B. H. Hong, and S. Iijima. Roll-to-roll production of 30-inch graphene films for transparent electrodes. *Nature Nanotechnology*, 5:574, 2010.

[13] S. Stankovich, D. A. Dikin, G. H. B. Dommett, K. M. Kohlhaas, E. J. Zimney, E. A. Stach, R. D. Piner, S. T. Nguyen, and R. S. Ruoff. Graphene-based composite materials. *Nature*, 442(7100):282–286, 2006.

[14] D. A. Dikin, S. Stankovich, E. J. Zimney, R. D. Piner, G. H. B. Dommett, G. Evmenenko, S. B. T. Nguyen, and R. S. Ruoff. Preparation and characterization of graphene oxide paper. *Nature*, 448(7152):457–460, 2007.

[15] A. A. Balandin, S. Ghosh, W. Bao, I. Calizo, D. Teweldebrhan, F. Miao, and C. N. Lau. Superior thermal conductivity of single-layer graphene. *Nano Letters*, 8(3):902–907, 2008.

[16] Y. Zhang, S. Huang, N. Wang, J. Bao, S. Sun, M. Edwards, X. Fu, W. Yue, X. Lu, and Y. Zhang. 2d heat dissipation materials for microelectronics cooling applications. In *Semiconductor Technology International Conference (CSTIC), 2016 China*, pages 1–4. IEEE, 2016.

[17] R. R. Nair, P. Blake, A. N. Grigorenko, K. S. Novoselov, T. J. Booth, T. Stauber, N. M. R. Peres, and A. K. Geim. Fine structure constant defines visual transparency of graphene. *Science*, 320(5881):1308–1308, 2008.

[18] C. Guo, X. Kong, and H. Ji. Hot-roll-pressing mediated transfer of chemical vapor deposition graphene for transparent and flexible touch screen with low sheet-resistance. *Journal of Nanoscience and Nanotechnology*, 18(6):4337–4342, 2018.

[19] W. Han, R. K. Kawakami, M. Gmitra, and J. Fabian. Graphene spintronics. *Nature Nanotechnology*, 9(10):794–807, 2014.

[20] A. S. Mayorov, R. V. Gorbachev, S. V. Morozov, L. Britnell, R. Jalil, L. A. Ponomarenko, P. Blake, K. S. Novoselov, K. Watanabe, and T. Taniguchi. Micrometer-scale ballistic transport in encapsulated graphene at room temperature. *Nano Letters*, 11(6):2396–2399, 2011.

[21] L. Banszerus, M. Schmitz, S. Engels, M. Goldsche, K. Watanabe, T. Taniguchi, B. Beschoten, and C. Stampfer. Ballistic transport exceeding 28 μm in cvd grown graphene. *Nano Letters*, 16(2):1387–1391, 2016.

[22] S. Chen, Z. Han, M. M. Elahi, K. M. M. Habib, L. Wang, B. Wen, Y. Gao, T. Taniguchi, K. Watanabe, and J. Hone. Electron optics with pn junctions in ballistic graphene. *Science*, 353(6307):1522–1525, 2016.

[23] J. Dauber, A. A. Sagade, M. Oellers, K. Watanabe, T. Taniguchi, D. Neumaier, and C. Stampfer. Ultra-sensitive hall sensors based on graphene encapsulated in hexagonal boron nitride. *Applied Physics Letters*, 106(19), 2015. cited By 13.

[24] E. Guerriero, P. Pedrinazzi, A. Mansouri, O. Habibpour, M. Winters, N. Rorsman, A. Behnam, E. A. Carrion, A. Pesquera, and A. Centeno. High-gain graphene transistors with a thin alox top-gate oxide. *Scientific Reports*, 7, 2017.

[25] E. V. Castro, K. S. Novoselov, S. V. Morozov, N. M. R. Peres, J. M. B. L. Dos Santos, J. Nilsson, F. Guinea, A. K. Geim, and A. H. Castro Neto. Biased bilayer graphene: semiconductor with a gap tunable by the electric field effect. *Physical Review Letters*, 99(21):216802, 2007.

[26] S. Lee, K. Lee, and Z. Zhong. Wafer scale homogeneous bilayer graphene films by chemical vapor deposition. *Nano Letters*, 10(11):4702–4707, 2010.

[27] S. Nie, W. Wu, S. Xing, Q. Yu, J. Bao, S.-S. Pei, and K. F. McCarty. Growth from below: bilayer graphene on copper by chemical vapor deposition. *New Journal of Physics*, 14(9):093028, 2012.

[28] C. R. Dean, A. F. Young, I. Meric, C. Lee, L. Wang, S. Sorgenfrei, K. Watanabe, T. Taniguchi, P. Kim, K. L. Shepard, and J. Hone. Boron nitride substrates for high-quality graphene electronics. *Nature Nanotechnology*, 5(10):722–726, 2010.

[29] A. N. Rudenko, S. Brener, and M. I. Katsnelson. Intrinsic charge carrier mobility in single-layer black phosphorus. *Physical review letters*, 116(24):246401, 2016.

[30] L. Li, F. Yang, G. J. Ye, Z. Zhang, Z. Zhu, W. Lou, X. Zhou, L. Li, K. Watanabe, and T. Taniguchi. Quantum hall effect in black phosphorus two-dimensional electron system. *Nature Nanotechnology*, 11(7):593–597, 2016.

[31] K. F. Mak and J. Shan. Photonics and optoelectronics of 2d semiconductor transition metal dichalcogenides. *Nature Photonics*, 10(4):216–226, 2016.

[32] O. Bubnova. Transition metal dichalcogenides: A topological phase in 2d. *Nature Nanotechnology*, 2017.

[33] S. Manzeli, D. Ovchinnikov, D. Pasquier, O. V. Yazyev, and A. Kis. 2d transition metal dichalcogenides. *Nature Reviews Materials*, 2(EPFL-REVIEW-229154):17033, 2017.

[34] A. H. Castro Neto, F. Guinea, N. M. R. Peres, K. S. Novoselov, and A. K. Geim. The electronic properties of graphene. *Rev. Mod. Phys.*, 81:109–162, Jan 2009.

[35] R. A. Nistor, M. A. Kuroda, A. A. Maarouf, and G. J. Martyna. Doping of adsorbed graphene from defects and impurities in sio 2 substrates. *Physical Review B - Condensed Matter and Materials Physics*, 86(4), 2012.

[36] S. K. Hong, S. M. Song, O. Sul, and B. J. Cho. Carboxylic group as the origin of electrical performance degradation during the transfer process of cvd growth graphene. *Journal of The Electrochemical Society*, 159(4):K107–K109, 2012.

[37] S. Kim, J. Nah, I. Jo, D. Shahrjerdi, L. Colombo, Z. Yao, E. Tutuc, and S. K. Banerjee. Realization of a high mobility dual-gated graphene field-effect transistor with al2o3 dielectric. *Applied Physics Letters*, 94(6):062107, 2009.

[38] M. Neek-Amal and F. M. Peeters. Lattice thermal properties of graphane: thermal contraction, roughness, and heat capacity. *Physical Review B*, 83(23):235437, 2011.

[39] J. H. Seol, I. Jo, A. L. Moore, L. Lindsay, Z. H. Aitken, M. T Pettes, X. Li, Z. Yao, R. Huang, and D. Broido. Two-dimensional phonon transport in supported graphene. *Science*, 328(5975):213–216, 2010.

[40] S. Yiğen, V. Tayari, J. O. Island, J. M. Porter, and A. R. Champagne. Electronic thermal conductivity measurements in intrinsic graphene. *Physical Review B*, 87(24):241411, 2013.

[41] E. H. Hwang, S. Adam, and S. Das Sarma. Carrier transport in two-dimensional graphene layers. *Physical Review Letters*, 98(18):186806, 2007.

[42] R. Bistritzer and A. H. MacDonald. Electronic cooling in graphene. *Physical Review Letters*, 102(20):206410, 2009.

[43] S. S. Kubakaddi. Interaction of massless dirac electrons with acoustic phonons in graphene at low temperatures. *Physical Review B*, 79(7):075417, 2009.

[44] J. K. Viljas and T. T. Heikkil. Electron-phonon heat transfer in monolayer and bilayer graphene. *Physical Review B*, 81(24):245404, 2010.

[45] A. A. Abrikosov. *Fundamentals of the Theory of Metals*. Courier Dover Publications, 2017.

[46] T. Löfwander and M. Fogelström. Impurity scattering and mott's formula in graphene. *Physical Review B*, 76(19):193401, 2007.

[47] N. Colthup. *Introduction to infrared and Raman spectroscopy*. Elsevier, 2012.

[48] A. C. Ferrari, J. C. Meyer, V. Scardaci, C. Casiraghi, M. Lazzeri, F. Mauri, S. Piscanec, D. Jiang, K. S. Novoselov, S. Roth, and A. K. Geim. Raman spectrum of graphene and graphene layers. *Physical Review Letters*, 97(18), 2006.

[49] L. M. Malard, M. A. Pimenta, G. Dresselhaus, and M. S. Dresselhaus. Raman spectroscopy in graphene. *Physics Reports*, 473(5):51 – 87, 2009.

[50] L. Wang, I. Meric, P. Y. Huang, Q. Gao, Y. Gao, H. Tran, T. Taniguchi, K. Watanabe, L. M. Campos, D. A. Muller, J. Guo, P. Kim, J. Hone, K. L. Shepard, and C. R. Dean. One-dimensional electrical contact to a two-dimensional material. *Science*, 342(6158):614–617, 2013.

[51] K. S. Kim, Y. Zhao, H. Jang, S. Y. Lee, J. M. Kim, K. S. Kim, J.-H. Ahn, P. Kim, J.-Y. Choi, and B. H. Hong. Large-scale pattern growth of graphene films for stretchable transparent electrodes. *Nature*, 457(7230):706–710, 2009.

[52] I. Vlassiouk, M. Regmi, P. Fulvio, S. Dai, P. Datskos, G. Eres, and S. Smirnov. Role of hydrogen in chemical vapor deposition growth of large single-crystal graphene. *ACS Nano*, 5(7):6069–6076, 2011.

[53] J. Sun, M. T. Cole, N. Lindvall, K. B. K. Teo, and A. Yurgens. Noncatalytic chemical vapor deposition of graphene on high-temperature substrates for transparent electrodes. *Applied Physics Letters*, 100(2):022102, 2012.

[54] H. Zhou, W. J. Yu, L. Liu, R. Cheng, Y. Chen, X. Huang, Y. Liu, Y. Wang, Y. Huang, and X. Duan. Chemical vapour deposition growth of large single crystals of monolayer and bilayer graphene. *Nature Communications*, 4, 2013.

[55] A. Mohsin, L. Liu, P. Liu, W. Deng, I. N. Ivanov, G. Li, O. E. Dyck, G. Duscher, J. R. Dunlap, K. Xiao, and G. Gu. Synthesis of millimeter-size hexagon-shaped graphene single crystals on resolidified copper. *ACS Nano*, 7(10):8924–8931, 2013.

[56] M. Ohring. *Materials Science of Thin Films*. Academic Press, 2002.

[57] J. Sun, N. Lindvall, M. T. Cole, K. T. T. Angel, W. Teng, K. B. K. Teo, D. H. C. Chua, L. Johan, and A. Yurgens. Low partial pressure chemical vapor deposition of graphene on copper. *IEEE Transactions Nanotechnology*, 11(2):255–260, 2012.

[58] Y. Hao, M. S. Bharathi, L. Wang, Y. Liu, H. Chen, S. Nie, X. Wang, H. Chou, C. Tan, B. Fallahazad, H. Ramanarayan, C. W. Magnuson, E. Tutuc, B.I. Yakobson, K. F. McCarty, Y.-W. Zhang, P. Kim, J. Hone, L. Colombo, and R. S. Ruoff. The role of surface oxygen in the growth of large single-crystal graphene on copper. *Science*, 342(6159):720–723, 2013.

[59] J. Sun, M. T. Cole, N. Lindvall, K. B. K. Teo, and A. Yurgens. Noncatalytic chemical vapor deposition of graphene on high-temperature substrates for transparent electrodes. *Applied Physics Letters*, 100(2):022102, 2012.

[60] J. W. Suk, A. Kitt, C. W. Magnuson, Y. Hao, S. Ahmed, J. An, A. K. Swan, B. B. Goldberg, and R. S. Ruoff. Transfer of cvd-grown monolayer graphene onto arbitrary substrates. *ACS Nano*, 5(9):6916–6924, 2011.

[61] L. Gao, W. Ren, H. Xu, L. Jin, Z. Wang, T. Ma, L.-P. Ma, Z. Zhang, Q. Fu, L.-M. Peng, X. Bao, and H.-M. Cheng. Repeated growth and bubbling transfer of graphene with millimetre-size single-crystal grains using platinum. *Nature Communications*, 3:699, 2012.

[62] A. C. Ferrari and D. M. Basko. Raman spectroscopy as a versatile tool for studying the properties of graphene. *Nature Nanotechnology*, 8(4):235–246, 2013.

[63] K. S. Novoselov, S. V. Morozov, T. M. G. Mohinddin, L. A. Ponomarenko, D. C. Elias, R. Yang, I. I. Barbolina, P. Blake, T. J. Booth, D. Jiang, J. Giesbers, E. W. Hill, and A. K. Geim. Electronic properties of graphene. *Physica Status Solidi (B) Basic Research*, 244(11):4106–4111, 2007.

[64] S. Z. Butler, S. M. Hollen, L. Cao, Y. Cui, J. A. Gupta, H. R. Gutiérrez, T. F. Heinz, S. S. Hong, J. Huang, and A. F. Ismach. Progress, challenges, and opportunities in two-dimensional materials beyond graphene. *ACS nano*, 7(4):2898–2926, 2013.

[65] A. K. Geim and I. V. Grigorieva. Van der waals heterostructures. *Nature*, 499(7459):419–425, 2013.

[66] Y. Kubota, K. Watanabe, O. Tsuda, and T. Taniguchi. Hexagonal boron nitride single crystal growth at atmospheric pressure using ni cr solvent. *Chemistry of Materials*, 20(5):1661–1663, 2008.

[67] P. J. Zomer, M. H. D. Guimarães, J. C. Brant, N. Tombros, and B. J. van Wees. Fast pick up technique for high quality heterostructures of bilayer graphene and hexagonal boron nitride. *Applied Physics Letters*, 105(1):013101, 2014.

[68] L. Banszerus, M. Schmitz, S. Engels, J. Dauber, M. Oellers, F. Haupt, K. Watanabe, T. Taniguchi, B. Beschoten, and C. Stampfer. Ultrahigh-mobility graphene devices from chemical vapor deposition on reusable copper. *Science Advances*, 1(6):e1500222, 2015.

[69] S. J. Haigh, A. Gholinia, R. Jalil, S. Romani, L. Britnell, D. C. Elias, K. S. Novoselov, L. A. Ponomarenko, A. K. Geim, and R. Gorbachev.

Cross-sectional imaging of individual layers and buried interfaces of graphene-based heterostructures and superlattices. *Nature Materials*, 11(9):764–767, 2012. cited By 283.

[70] K. Slezakova, S. Morais, and M. do Carmo Pereira. *Atmospheric nanoparticles and their impacts on public health.* InTech, 2013.

[71] D. G. Purdie, A. C. Ferrari, and A. Lombardo. Blister cleaning for graphene encapsulated in hexagonal boron nitride. In *Graphene Week 2017*, page 361.

[72] K. H. Lee, H.-J. Shin, J. Lee, I.-Y. Lee, G.-H. Kim, J.-Y. Choi, and S.-W. Kim. Large-scale synthesis of high-quality hexagonal boron nitride nanosheets for large-area graphene electronics. *Nano Letters*, 12(2):714–718, 2012.

[73] V. Kale and T. Riley. A production parylene coating process for hybrid microcircuits. *IEEE Transactions on Parts, Hybrids, and Packaging*, 13(3):273–279, 1977.

[74] http://scscoatings.com/. Last accessed Dec. 2017.

[75] B. E. Rapp, A. Voigt, M. Dirschka, and K. Länge. Deposition of ultrathin parylene c films in the range of 18 nm to 142 nm: Controlling the layer thickness and assessing the closeness of the deposited films. *Thin Solid Films*, 520(15):4884–4888, 2012.

[76] S. S. Sabri, P. L. Lvesque, C. M. Aguirre, J. Guillemette, R. Martel, and T. Szkopek. Graphene field effect transistors with parylene gate dielectric. *Applied Physics Letters*, 95(24):242104, 2009.

[77] S. F. Chowdhury, S. Sonde, S. Rahimi, L. Tao, and D. Banerjee, S.and Akinwande. Improvement of graphene field-effect transistors by hexamethyldisilazane surface treatment. *Applied Physics Letters*, 105(3):033117, 2014.

[78] R. Han, Y. Zhang, D. Coquillat, H. Videlier, W. Knap, and E. Brown. A 280-ghz schottky diode detector in 130-nm digital cmos. *IEEE Journal of Solid-State Circuits*, 46(11):2602–2612, 2011.

[79] S. Boppel, A. Lisauskas, M. Mundt, D. Seliuta, L. Minkevicius, I. Kasalynas, G. Valusis, M. Mittendorff, S. Winnerl, and V. Krozer. Cmos integrated antenna-coupled field-effect transistors for the detection of radiation from 0.2 to 4.3 thz. *IEEE transactions on microwave theory and techniques*, 60(12):3834–3843, 2012.

[80] A. J. Miller, S. W. Nam, J. M. Martinis, and A. V Sergienko. Demonstration of a low-noise near-infrared photon counter with multiphoton discrimination. *Applied Physics Letters*, 83(4):791–793, 2003.

[81] L. S. Kuzmin. *Cold-electron bolometer.* InTech, 2012.

[82] A. Skalare, W. R. McGrath, B. Bumble, H. G. LeDuc, P. J. Burke, A. A. Verheijen, R. J. Schoelkopf, and D. E. Prober. Large bandwidth and low noise in a diffusion-cooled hot-electron bolometer mixer. *Applied physics letters*, 68(11):1558–1560, 1996.

[83] A. A. Generalov, M. A. Andersson, X. Yang, A. Vorobiev, and J. Stake. A 400-ghz graphene fet detector. *IEEE Transactions on Terahertz Science and Technology*, 7(5):614–616, 2017.

[84] J. Yan, M. H. Kim, J. A. Elle, A. B. Sushkov, G. S. Jenkins, H. M. Milchberg, M. S. Fuhrer, and H. D. Drew. Dual-gated bilayer graphene hot-electron bolometer. *Nature Nanotechnology*, 7(7):472–478, 2012.

[85] X. Xu, N. M. Gabor, J. S. Alden, A. M. van der Zande, and P. L. McEuen. Photo-thermoelectric effect at a graphene interface junction. *Nano Letters*, 10(2):562–566, 2010.

[86] N. M. Gabor, J. C. W. Song, Q. Ma, N. L. Nair, T. Taychatanapat, K. Watanabe, T. Taniguchi, L. S. Levitov, and P. Jarillo-Herrero. Hot carrierassisted intrinsic photoresponse in graphene. *Science*, 334(6056):648–652, 2011.

[87] M. Freitag, T. Low, F. Xia, and P. Avouris. Photoconductivity of biased graphene. *Nature Photonics*, 7(1):53–59, 2013.

[88] K. L. Grosse, M.-H. Bae, F. Lian, E. Pop, and W. P. King. Nanoscale joule heating, peltier cooling and current crowding at graphene-metal contacts. *Nature Nanotechnology*, 6(5):287–290, 2011.

[89] L. Liu, S. M. Rahman, Z. Jiang, W. Li, and P. Fay. Advanced terahertz sensing and imaging systems based on integrated iii-v interband tunneling devices. *Proceedings of the IEEE*, 105(6):1020–1034, 2017.

[90] F. Schuster, D. Coquillat, H. Videlier, M. Sakowicz, F. Teppe, L. Dussopt, B. Giffard, T. Skotnicki, and W. Knap. Broadband terahertz imaging with highly sensitive silicon cmos detectors. *Optics Express*, 19(8):7827–7832, 2011.

[91] D. Spirito, D. Coquillat, S. L. De Bonis, A. Lombardo, M. Bruna, A. C. Ferrari, V. Pellegrini, A. Tredicucci, W. Knap, and M. S. Vitiello. High performance bilayer-graphene terahertz detectors. *Applied Physics Letters*, 104(6):061111, 2014.

[92] V. H. Rumsey. *Frequency Independent Antennas.* Academic Press, 1966.

[93] M. J. E. Golay. A pneumatic infra-red detector. *Review of Scientific Instruments*, 18(5):357–362, 1947.

[94] V. Dobrovolsky and F. Sizov. A room temperature, or moderately cooled, fast thz semiconductor hot electron bolometer. *Semiconductor Science and Technology*, 22(2):103, 2007.

[95] M. A. Tarasov, L. S. Kuzmin, V. S. Edelman, S. Mahashabde, and P. de Bernardis. Optical response of a cold-electron bolometer array integrated in a 345-ghz cross-slot antenna. *IEEE transactions on Applied Superconductivity*, 21(6):3635–3639, 2011.

[96] T. Müller, F. Xia, and P. Avouris. Graphene photodetectors for high-speed optical communications. *Nature Photonics*, 4(5):297–301, 2010.

[97] A. A. Balandin. Low-frequency 1/f noise in graphene devices. *Nature Nanotechnology*, 8(8):549–555, 2013.

[98] A. C. Betz, S. H. Jhang, E. Pallecchi, R. Ferreira, G. Feve, J. M. Berroir, and B. Plaçais. Supercollision cooling in undoped graphene. *Nature Physics*, 9(2):109–112, 2013.

[99] A. C. Betz, F. Vialla, D. Brunel, C. Voisin, M. Picher, A. Cavanna, A. Madouri, G. Féve, J. M. Berroir, B. Plaçais, and E. Pallecchi. Hot electron cooling by acoustic phonons in graphene. *Physical Review Letters*, 109(5):056805, 2012.

[100] Godovsky Y. *Thermophysical properties of polymers.* Springer Science and Business Media, 1992.